J. Fluid Mech. (1983), *vol.* 131, *pp.* 123–153
Printed in Great Britain

On the structure of turbulent flow over a progressive water wave: theory and experiment in a transformed wave-following coordinate system. Part 2

By CHIN-TSAU HSU

Fluid Mechanics Department, TRW Defense and Space Systems Group, Redondo Beach, California 90278

AND EN YUN HSU

Department of Civil Engineering, Stanford University, Stanford, California 94305

(Received 23 November 1981 and in revised form 8 December 1982)

This experimental study extends our earlier work (Hsu, Hsu & Street 1981) on $U_\infty/c = 1.54$ to $U_\infty/c = 0.88$, 1.10, 1.36 and 1.87, where U_∞ is the mean-free-stream wind velocity and c is the celerity of the water wave. This was accomplished by changing the speed of the turbulent wind, while the water wave was maintained at a frequency of 1.0 Hz and wave slope of 0.1. The consistency between the results of the present and earlier experiments is established. The experimental results indicate that the mean velocity of the typical log-linear profile basically follows the waveform. However, the surface condition for the wind is regarded as supersmooth because the mean turbulent shear stress supported by the current is relatively lower than that supported by a smooth flat plate. The structure of the wave-induced velocity fields is found to be very sensitive to the height of the critical layer. When the critical height is high enough that most of the wave-induced flow in the turbulent boundary layer is below the critical layer, the structure of the wave-induced velocity field is strongly affected by the Stokes layer, which under the influence of the turbulence can have thickness comparable to the boundary-layer thickness. When the critical height is low enough that most of the wave-induced flow in the boundary layer is above the critical layer, the structure of the wave-induced velocity fields is then strongly affected by the critical layer. The structure of the critical layer is found to be nonlinear and turbulently diffusive. This implies that the inclusion of both the nonlinear and the turbulent terms in the wave-perturbed momentum equations is essential to success in the numerical modelling. The response of the turbulent Reynolds stresses to the wave is found to depend on the flow regimes near the interface or in the boundary layer. Near the interface, the wave-induced turbulent Reynolds stresses are found to be produced mainly from the stretching and changing in the direction of the turbulent velocity fluctuations due to the surface displacements. In the boundary layer, the eddy-viscosity-type relation between the wave-induced turbulent Reynolds stresses and the wave-induced velocities as found in Hsu *et al.* (1981) for $U_\infty/c = 1.54$ is also found to hold for the other U_∞/c values of this study.

1. Introduction

In our earlier paper (Hsu, Hsu & Street 1981, hereinafter referred to as I), we reported the turbulent airflow structure over a progressive water wave $\tilde{\eta}(x, t)$, as measured in a transformed wave-following coordinate system (x^*, y^*, z^*) given by

$$x = x^*, \tag{1.1a}$$

$$y = y^* + f(y^*)\,\tilde{\eta}, \tag{1.1b}$$

$$z = z^*, \tag{1.1c}$$

where (x, y, z) is a Cartesian coordinate system with x in the wave propagation and wind direction, y in the vertical direction measured form the mean water level and z in the horizontal direction normal to x. The function $f(y^*)$ was chosen to be

$$f(y^*) = \frac{\sinh(kH - ky^*)}{\sinh kH}, \tag{1.2}$$

where k is the wavenumber and H is the height from the mean water level to the channel roof of the experimental facility. Apparently $y^* =$ constant represents a streamline of potential flow over the wave and $y^* = 0$ corresponds to the air–water interface $y = \tilde{\eta}$. Note that $f(y^*) \to e^{-ky^*}$ when $H \to \infty$. In I, the mean free-stream wind velocity U_∞ is 2.40 m/s and the mechanically generated water wave has a frequency of 1 Hz, which gives the wave celerity $c = 1.56$ m/s and the wavenumber $k = 4.03\ \mathrm{m}^{-1}$. The wave slope ka is 0.107, where a is the wave amplitude.

The main results found in I were as follows.

(*a*) The mean flow basically follows the waveform; hence the transformed wave-following frame naturally provides a better representation of the airflowfields than a fixed-frame representation.

(*b*) The mean flow observed in (x^*, y^*, z^*) has structure similar to that of a turbulent boundary-layer flow over a smooth flat plate.

(*c*) The development of the surface drift current tends to release a portion of the wind stress so that the current-supported wind stress is smaller than that supported by a smooth flat plate.

(*d*) The production of the wave-associated Reynolds stress $-\overline{\tilde{u}\tilde{v}}(y^*)$ is mostly conducted at the vicinity of the interface where the value of $-\overline{\tilde{u}\tilde{v}}$ was found to increase rapidly.

(*e*) The measured wave-induced velocities and wave-induced turbulent Reynolds stresses indicate that an eddy-viscosity relationship exists between them.

(*f*) The eddy viscosity for the wave-induced flowfields is dramatically modified by the propagating behaviour of the wave.

Based on the results of I and with the aid of the pressure data of Yu, Hsu & Street (1973), Hsu, Hsu & Street (1982) then estimated the complete momentum and energy budgets of the air–water interface coupled system. They found that the wave receives more than 90 % of the total energy transfer across the interface while the waveform supported only about 44 % of the total momentum transfer across the interface, under those laboratory conditions. The most significant result was the experimental confirmation of the exact expression for the momentum transfer to the wave, i.e.

$$\overline{M}_{xw} = \overline{\tilde{p}\frac{\partial\tilde{\eta}}{\partial x}}\bigg|_{y^*=-\delta_0} + \overline{\rho\tilde{r}_{11}\frac{\partial\tilde{\eta}}{\partial x}}\bigg|_{y^*=-\delta_0} = -\overline{\rho\tilde{u}\tilde{v}}\bigg|_{y^*=-\delta_0} + \overline{\rho\tilde{\eta}\frac{\partial}{\partial y}\tilde{r}_{12}}\bigg|_{y^*=-\delta_0}, \tag{1.3}$$

where $\tilde{p}$ is the wave-induced pressure, $\tilde{r}_{ij}$ $(i, j = 1, 2)$ is the wave-induced turbulent Reynolds stress, ρ is the air density and δ_0 is the viscous sublayer thickness. However, the momentum transfer by $\tilde{r}_{11}$ is practically zero because the phase of $\tilde{r}_{11}$ approaches 0° when $y^* \to \delta_0$ and the momentum transfer by $\tilde{r}_{12}$ (last term of (1.3)) is only about 10 % of $\bar{M}_{xw}$. Hence the wind turbulence contributes directly only a negligible amount of the wind momentum supported by the wave. From the energy budget, they also found that the energy received by the wave is mainly delivered by the wave-induced pressure and that the direct energy input by the wind turbulence is insignificant. However, the momentum and energy transfer by the wave-induced pressure is found to be considerably larger than that predicted by Miles' (1957) theory, implying that the turbulent effect is more likely to modify the wave-induced flow structure to enhance the transfer by the wave-induced pressure.

As the above results were for $U_\infty/c = 1.54$, it becomes obvious that in order to obtain a more systematic insight to the structure of the wave-induced flow, observations of the flowfields at different U_∞/c have to be made. In this paper, we report the results of the wind measurements at $U_\infty/c = 0.88$, 1.10, 1.36 and 1.87 obtained by changing the wind speeds while practically maintaining the same wave conditions as in I. The structure of our text is as follows. In §§2 and 3 we review briefly the decomposition techniques and the experimental conditions that are essential to the complete presentation of the present work. The experimental results are then presented and discussed in §4, using our findings of I as guidelines. As implied from these experimental results, the general structure of the wave-induced flow is developed and discussed in §5 based on the velocity scales and lengthscales of the wave, the boundary-layer wind and the critical layer. The mechanism for the production of the wave-associated Reynolds stress $-\overline{\tilde{u}\tilde{v}}$ is also examined in §§4 and 5, but the balance of the momentum and energy budget is reserved for a separate paper. Finally, §6 offers a summary of our conclusions.

2. Averaging and decomposition

In a turbulent flow over an organized progressive water wave, a flow quantity g, which can be the velocity $u_i = (u, v, w)$, the pressure p or the turbulent Reynolds stress $u_i' u_j'$, etc., usually contains a mean-flow quantity, a wave-induced quantity and a background turbulent-fluctuation quantity. To obtain the mean-flow quantity, a time average is defined as

$$G(\boldsymbol{x}) = \bar{g}(\boldsymbol{x}) = \lim_{T\to\infty} \frac{1}{T} \int_{-\frac{1}{2}T}^{\frac{1}{2}T} g(\boldsymbol{x}, t)\, \mathrm{d}t, \tag{2.1}$$

where $\boldsymbol{x}$ is a vector representing the position during data sampling. The notation G is used when g represents a single-lettered quantity such as u, v and p etc.; $\bar{g}$ is then used for a product quantity such as $\overline{u_i' u_j'}$. To eliminate the turbulent fluctuation, a phase average is defined as

$$\langle g \rangle (\boldsymbol{x}, t) = \lim_{N\to\infty} \frac{1}{2N+1} \sum_{n=-N}^{N} g(\boldsymbol{x}, t + n\tau), \tag{2.2}$$

where τ is the wave period. Now, the wave-induced flow quantity $\tilde{g}$ can be found from

$$\tilde{g} = \langle g \rangle - \bar{g}. \tag{2.3}$$

Run	U_∞ (m/s)	u_* (cm/s)	C	ka	U_∞/c	c/u_*	$k\delta_0$	ky_c^*
1	1.37	4.3	13.6	0.106	0.88	36.3	0.015	∞
2	1.72	5.6	11.3	0.107	1.10	27.9	0.012	0.47
3	2.12	7.3	9.9	0.105	1.36	21.4	0.0088	0.085
I†	2.40	8.5	8.6	0.107	1.54	18.2	0.0076	0.034
4	2.92	11.0	7.1	0.115	1.87	14.2	0.0057	0.012

† The run of Hsu *et al.* (1981) referred to as I.

TABLE 1. Experimental conditions of the wind and the wave

As a result, g is decomposed into

$$g = \bar{g} + \tilde{g} + g', \tag{2.4}$$

where g' is the turbulent-fluctuation quantity. The general properties of the time and the phase averages can be found in Hussain & Reynolds (1970).

In (2.1) and (2.2), the position $\boldsymbol{x}$ has to be specified during the course of the averaging. In fixed-frame analyses or measurements $\boldsymbol{x} = (x, y, z)$; in this study $\boldsymbol{x} = (x^*, y^*, z^*)$, where (x^*, y^*, z^*) is the transformed wave-following frame defined by (1.1) and (1.2). Here (x^*, y^*, z^*) remains constant during averaging, although the actual physical position of $\boldsymbol{x}$ changes with time. The advantages of using the transformed wave-following frame in representing the interface flow system with surface waves were discussed in detail in I.

It is noted that, in the present treatment, we transform only the coordinate system but not the flowfields. Hence, the velocity fields as well as the turbulent and viscous stresses are expressed in the component directions of the Cartesian coordinate system, although their variations are described by (x^*, y^*, z^*). We also assume the phase-averaged airflow to be two-dimensional and stationary; hence $\bar{g} = \bar{g}(x^*, y^*)$ and $\tilde{g} = \tilde{g}(x^*, y^*, t^*)$. We assume that the dependence of $\bar{g}$ on x^* is mainly of boundary-layer type and is much weaker than the dependence of $\tilde{g}$ on x^* resulting from the surface-wave undulations. For the boundary-layer flow we also have $\partial\bar{g}/\partial x^* \ll \partial\bar{g}/\partial y^*$.

3. Experiments

The experiments were performed in the Stanford Wind, Water-Waves Research Facility. The experimental conditions were practically the same as those in I, except for the difference in the wind speeds, viz the mechanically generated water wave is of 1 Hz; the height of airflow is 0.97 m; the water depth is about 1 m to ensure a deep-water wave, and the data-taking station was located at $x = 13$ m from the air inlet of the channel. For the present measurements, four runs with different mean free-stream wind velocities U_∞ at 1.37, 1.72, 2.12 and 2.92 m/s were made. The reduced wave amplitudes for the four runs were found to differ slightly. The values of U_∞ as well as of U_∞/c and ka (the wave slope) are listed in table 1. For reference, the corresponding values from I are also recorded in table 1.

As in I, the air-velocity components in the x- and y-directions were measured by a cross hot-film probe operated in the wave-following frame using a wave-follower system; the wave displacement was measured by a capacitance-type wave-height gauge, and the probe calibrations and the data acquisition and reduction were

performed digitally in an HP2100A minicomputer. The details of these systems as well as their associated uncertainties were discussed in I and are not elaborated upon here.

4. Experimental results

4.1. *Format of presentation*

The flow quantity is generally presented in profile distribution as a function of y^*. The profiles are usually in non-dimensional form; typically U_∞ and U_∞^2 are used to normalize the velocities and the Reynolds stresses respectively, and the ordinate y^* is normalized by k. However, when interpretation in wall coordinates is required, the friction velocity u_* and the viscous length scale ν/u_* are used for normalization. The wave-induced quantity is expressed in terms of the amplitude and phase distributions given by

$$\tilde{g}(x^*, y^*, t) = |\hat{g}| \cos(kx^* - \omega t + \theta_{\tilde{g}}) + \text{harmonics}, \tag{4.1}$$

where $|\hat{g}|$ is the amplitude and $\theta_{\tilde{g}}$ is the phase-lag angle of the fundamental mode. The phase lag is with respect to time using $\tilde{\eta}$ as a reference, i.e. $\tilde{\eta}$ is represented by

$$\tilde{\eta}(x^*, t) = a \cos(kx^* - \omega t) + \text{harmonics}, \tag{4.2}$$

where ω is the wave frequency.

4.2. *Mean flowfields*

As followed from I, the mean horizontal velocity profiles measured in this study fit well the wake-modified log-linear distribution given by

$$\frac{U}{u_*} = \frac{1}{k_0} \ln \frac{y^* u_*}{\nu} + C + \frac{W_c}{k_0} W\left(\frac{y^*}{\delta}\right). \tag{4.3}$$

Here $k_0 = 0.40$ is the von Kármán constant, ν is the air kinematic viscosity, C is the profile constant for surface roughness, W_c is the wake parameter, δ is the boundary-layer thickness and $W(y^*/\delta)$ is the wake distribution, which can be approximated by (Hinze 1975)

$$W\left(\frac{y^*}{\delta}\right) = 1 - \cos\frac{\pi y^*}{\delta}. \tag{4.4}$$

While W_c and δ are found to be almost the same as those of I and are not sensitive to the wind speeds, the values of u_* and C are found to depend strongly on the wind speeds. The values of u_* and C as well as the wind/wave coupling parameter c/u_* are given in table 1, together with the results obtained in I. The consistence between this study and I is obtained. The measured velocity profiles in terms of the wall coordinates $u^+ = U/u_*$ and $y^+ = y^* u_*/\nu$ are shown in figure 1. The drag coefficient C_D defined by $C_D = (u_*/U_\infty)^2$ is plotted against the Reynolds number $U_\infty x/\nu$ based on the wind fetch x in figure 2. Consistency among the results of this study, I and Yu *et al.* (1973) is found.

Since u_*^2 denotes the wind stress supported by mean surface (see Hsu *et al.* 1982) and C is the parameter to indicate the surface roughness condition, figure 2 indicates that the surface drag of the air–water interface at the low wind speeds of this study is lower than that of a smooth flat plate. This behaviour is also indicated by the higher

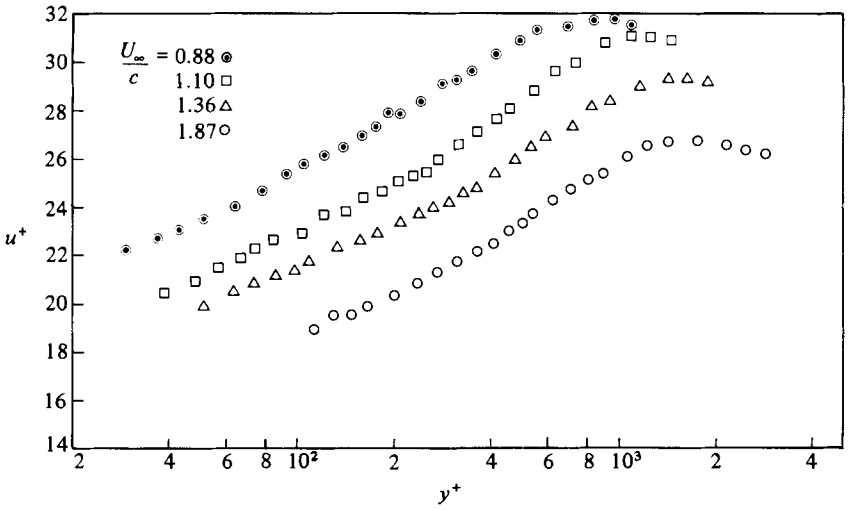

FIGURE 1. The mean horizontal velocity profiles in the wall coordinates $u^+ = U/u_*$ and $y^+ = y^* u_*/\nu$.

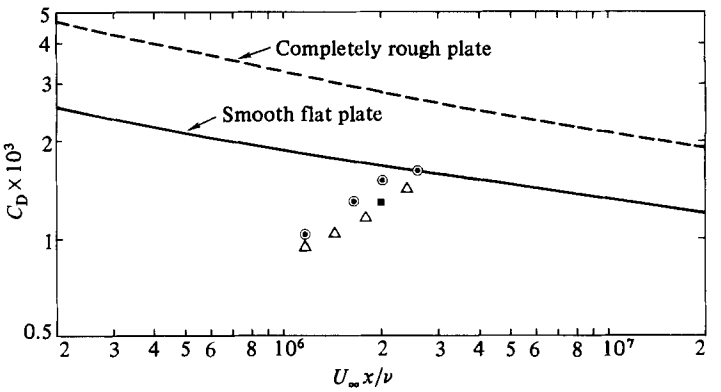

FIGURE 2. Wind-drag coefficient C_D as a function of Reynolds number $U_\infty x/\nu$. ⊙, Yu *et al.* (1973); ■, Hsu *et al.* (1981); △, this experiment.

values of C, since $C = 5.5$ for a smooth flat plate and decreases monotonically with increasing surface roughness. The air–water interface at the low wind speeds apparently behaves as a supersmooth surface as described by Csanady (1974), who demonstrated that the field measurements by Portman (1960) and Sheppard, Tribble & Garrett (1972) can have values of C as high as 30. The existence of the surface drift current seems to modify the wind velocity profile to have higher C by releasing a portion of the wind stress. This leads to lower u_* for the interface flow, and consequently the value of C is higher.

As the mean flow follows basically the waveform and the interface condition is aerodynamically smooth, we expect that there exists a thin viscous sublayer undulating with the waveform. The thickness δ_0 of the viscous sublayer is determined by $\delta_0 u_*/\nu = 10$ (Phillips 1977, p. 128); the non-dimensional values of $k\delta_0$ are given in table 1. Note that $k\delta_0 \ll ka$, i.e. the thickness of the viscous sublayer is much smaller than the wave amplitude.

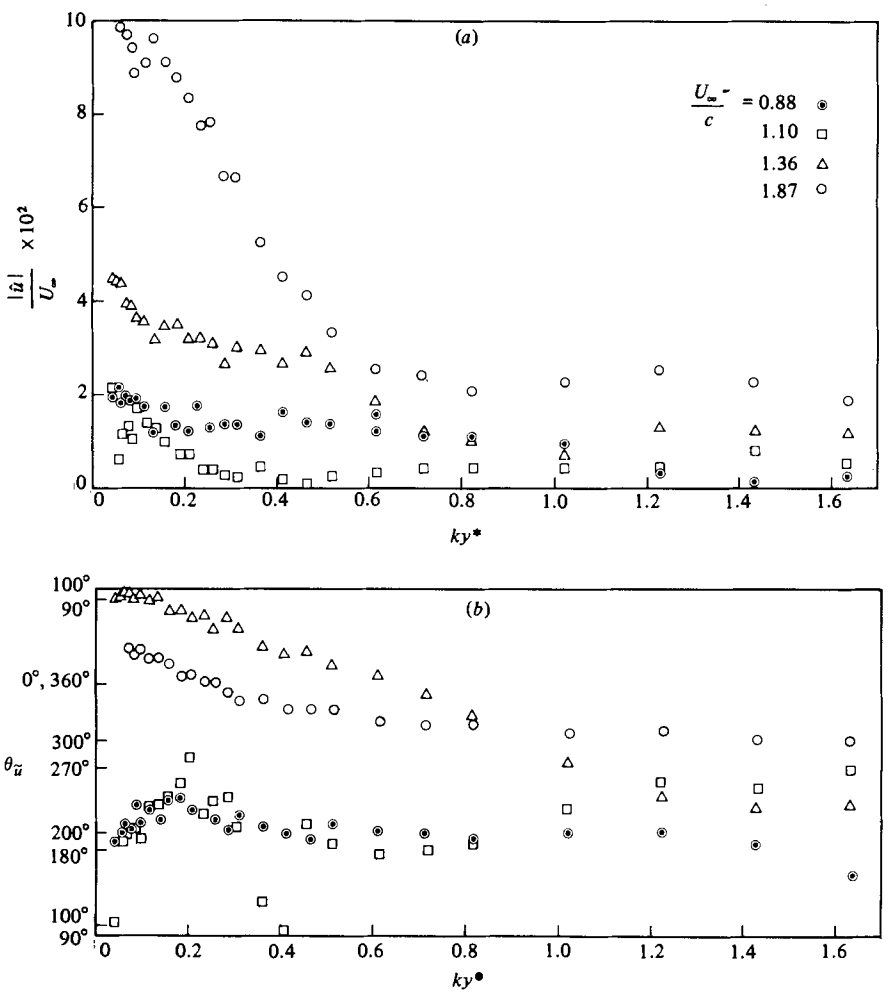

FIGURE 3. Profiles of the wave-induced horizontal velocity $\tilde{u}$: (*a*) amplitudes; (*b*) phases.

4.3. *Wave-induced flowfields*

The main objective of this study is to understand the structure of the wave-induced flow fields, knowing the structures of the mean wind and wave fields. Apparently, the wave-induced flow is dependent on the coupling parameters between the wind and the wave; these parameters are determined by the relative length scales and velocity scales of the wind to the wave. In this section, we present only the general characteristics of the wave-induced flow as obtained from the direct measurements, while the way in which the structures of the wave-induced flow vary with these coupling parameters is discussed in §5.

4.3.1. *Wave-induced velocities.* The amplitudes and the phase angles of the wave-induced velocities $\tilde{u}$ and $\tilde{v}$ are shown in figures 3 and 4. Before we examine the detailed features of $\tilde{u}$ and $\tilde{v}$, it is useful to notice that for the four runs of $U_\infty/c = 0.88$, 1.10, 1.36 and 1.87, the condition for the wave-induced flow ranges from entirely below a critical height at $U_\infty/c = 0.88$ to almost entirely above the critical height at $U_\infty/c = 1.87$. The critical height y_c^* is located at $U(y_c^*) - c = 0$. Without loss of generality, the case $U_\infty < c$ can be regarded as the critical height being at $y_c^* = \infty$.

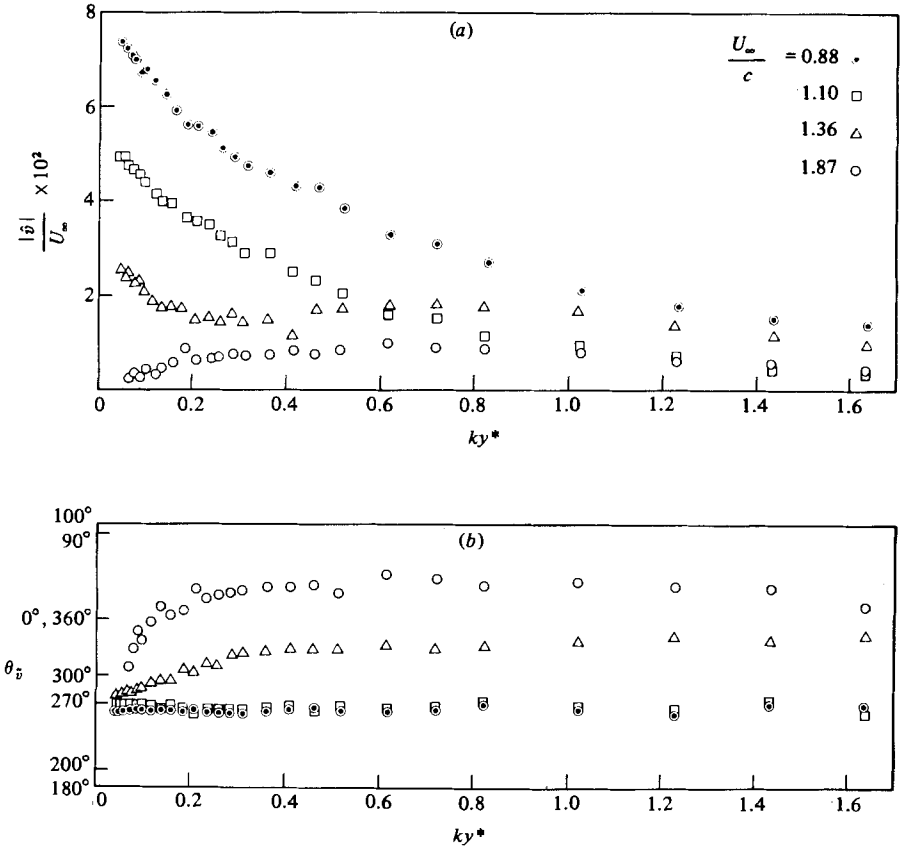

FIGURE 4. Profiles of the wave-induced vertical velocity $\tilde{v}$: (*a*) amplitudes; (*b*) phases.

The values of the critical height y_c^* are determined from the measured mean-velocity profiles, and the non-dimensional results ky_c^* are listed in table 1. In the following, we examine the wave-induced flow characteristics in two regions: one is near the interface below $ky^* = 0.5$ where the mean shear and the turbulent intensity are high and the mean turbulent Reynolds stress is almost constant, the other is near the free stream above $ky^* = 0.5$ where the turbulent shear is less important.

Near the interface, we find from figures 3 and 4 that the amplitudes $|\hat{v}|/U_\infty$ are much larger than the amplitudes $|\hat{u}|/U_\infty$ when $U_\infty/c = 0.88$ and 1.10, especially as ky^* approaches the interface; however, the opposite situation happens when $U_\infty/c = 1.36$ and 1.87. Note that the flow in this region is below the critical height when $U_\infty/c = 0.88$ and 1.10, and is mostly above the critical height when $U_\infty/c = 1.36$ and 1.87. Because the amplitude of $\tilde{v}$ is related very closely to the undulation of the mean streamlines as observed in a frame $x_c^* = x^* - ct$ travelling at the wave celerity, the above results suggest that the mean streamlines (phase-averaged streamlines) below the critical height follow the waveform very well, while those above the critical height are affected strongly by the critical layer. The implication is that if there exist cat's-eye patterns in the flow of these higher winds speeds, the centre of the cat's-eye is probably located in the troughs near the leeward side of the wave. The phase angles $\theta_{\tilde{v}}$ as shown in figure 4 (*b*) remain quite constant near the interface when $U_\infty/c = 0.88$ and 1.10. The variation of $\theta_{\tilde{v}}$ near the interface increases when U_∞/c increases.

However, $\theta_{\tilde{v}}$ approaches 270° for all runs when $ky^* \to 0$, which appears to be consistent with the interface boundary condition of $\tilde{v}$. On the other hand, the trend in the variations of $\theta_{\tilde{u}}$ with U_∞/c near the interface is more subtle than that of $\theta_{\tilde{v}}$. The values of $\theta_{\tilde{u}}$ do not approach a fixed value when $ky^* \to 0$; this behaviour is considered to be a consequence of the Stokes layer and the critical layer which is discussed later.

We now examine the wave-induced flow characteristics near the mean free stream where the mean velocity gradient (shear effect) and the turbulent mixing are small. Near the free stream, the wave-induced flow is expected to behave as a potential flow. This had been confirmed by our earlier measurements of I and is also indicated by the distributions of $\tilde{u}$ and $\tilde{v}$ shown in figures 3 and 4. Several features of $\tilde{u}$ and $\tilde{v}$ near the free stream are worth noting: (i) the amplitudes of $|\hat{u}|/U_\infty$ and $|\hat{v}|/U_\infty$ are of practically the same magnitude; (ii) the phase angles $\theta_{\tilde{u}}$ and $\theta_{\tilde{v}}$ are expected to remain almost constant at different ky^* – this situation is probably more true for $\theta_{\tilde{v}}$ which is less sensitive to the effect of the misalignment between the phase-averaged streamlines and the wave-following coordinates where $y^* =$ constant; (iii) the phase angles $\theta_{\tilde{u}}$ and $\theta_{\tilde{v}}$ for different values of U_∞/c depend on the undulation of the phase-averaged streamlines near $ky^* = 0.5$ before transmitting into the shear-free region near the free stream; (iv) the phase difference between $\theta_{\tilde{u}}$ and $\theta_{\tilde{v}}$ becomes 90° when ky^* becomes large.

The values of $\tilde{u}$ and $\tilde{v}$ in the proximity of the interface are of great interest since $-\overline{\tilde{u}\tilde{v}}$ at $y^* = \delta_0$ represents a good estimate of the momentum flux supported by the wave. The interface boundary conditions for $\tilde{u}$ and $\tilde{v}$ under the influence of the surface drift current U_0 are given to $O(ka)$ by (Phillips 1977, p. 95)

$$\tilde{u}(x^*, 0, t) = k(c + U_0)\,\tilde{\eta}, \tag{4.5a}$$

$$\tilde{v}(x^*, 0, t) = \frac{\partial \tilde{\eta}}{\partial t} + U_0 \frac{\partial \tilde{\eta}}{\partial x^*}. \tag{4.5b}$$

Because $c \gg U_0$, the estimate of U_0 is not crucial in (4.5); for the present study, we take $U_0 = 0.55u_*$ based on the measurements of Wu (1975). The amplitudes and the phase angles of $\tilde{u}$ and $\tilde{v}$ at $y^* = 0$ as determined by (4.5) are given in table 2. Since we have always $\theta_{\tilde{u}} = 0°$ and $\theta_{\tilde{v}} = 270°$ at $y^* = 0$, we find $-\overline{\tilde{u}\tilde{v}} = 0$ at $y^* = 0$ to $O(ka)^2$, which is a necessary condition if the interface represents a streamline, as demonstrated by Hsu *et al.* (1982). For comparisons, the values of $|\hat{u}|/U_\infty$, $|\hat{v}|/U_\infty$, $\theta_{\tilde{u}}$ and $\theta_{\tilde{v}}$ when $y^* \to 0$ are extrapolated from figures 3 and 4; they are listed in table 2, together with the values of $-\overline{\tilde{u}\tilde{v}}/U_\infty^2$ when $y^* \to 0$ as calculated by $-\overline{\tilde{u}\tilde{v}} = -\frac{1}{2}|\hat{u}||\hat{v}|\cos(\theta_{\tilde{u}} - \theta_{\tilde{v}})$. We want to emphasize that the extrapolation by $ky^* \to 0$ yields the inviscid limit outside the viscous sublayer when $k\delta_0$ is very small, not the limit value at $ky^* = 0$, i.e. our extrapolation results represent the values at $y^* = \delta_0$. We also notice that the value for $|\hat{v}|/U_\infty$ when $U_\infty/c = 1.87$ cannot be extrapolated directly from the profile shown in figure 4. Because the value of $|\hat{v}|/U_\infty$ is expected to increase rapidly when ky^* passes below the critical layer and approaches the interface, as suggested by the other three cases of $U_\infty/c = 0.88$, 1.10 and 1.36, the value of $|\hat{v}|/U_\infty$ at $y^* = \delta_0$ when $U_\infty/c = 1.87$ is determined alternatively by indirect extrapolation based on the parameter U_∞/c using the values of $|\hat{v}|/U_\infty$ at $y^* = \delta_0$ of $U_\infty/c = 0.88$, 1.10, 1.36 and 1.54. From table 2 it is clear that the values of $\tilde{u}$ and $\tilde{v}$ at $y^* = 0$ are different from those of $y^* \to 0$ as anticipated.

To obtain more insight into $\tilde{u}$ and $\tilde{v}$ near the interface, we review the predictions based on the inviscid quasi-laminar model of Miles (1957). The analysis of Benjamin

(*a*) Calculations from the interface boundary conditions (at $y^* = 0$)

Run	$\frac{\lvert\hat{u}\rvert}{U_\infty} \times 10^2$	$\theta_{\hat{u}}$	$\frac{\lvert\hat{v}\rvert}{U_\infty} \times 10^2$	$\theta_{\hat{v}}$
1	12.2	0°	11.9	270°
2	9.9	0°	9.5	270°
3	7.9	0°	7.5	270°
I‡	7.2	0°	6.7	270°
5	6.4	0°	5.9	270°

(*b*) Extrapolations from figures 3 and 4 (at $y^* = \delta_0$)

Run	$\frac{\lvert\hat{u}\rvert}{U_\infty} \times 10^2$	$\theta_{\tilde{u}}$	$\frac{\lvert\hat{v}\rvert}{U_\infty} \times 10^2$	$\theta_{\tilde{v}}$	$\frac{-\overline{\tilde{u}\tilde{v}}}{U_\infty^2} \times 10^4$
1	2.4	180°	8.0	270°	0
2	1.6	142°	5.6	270°	2.8
3	5.2	100°	3.1	270°	7.9
I‡	8.0	89°	2.4	270°	9.6
5	11.2	63°	1.1	270°	5.5

(*c*) Predictions from the inviscid quasi-laminar model of Miles (1957) (at $y^* = \delta_0$)

Run	$\frac{\lvert\hat{u}\rvert}{U_\infty} \times 10^2$	$\theta_{\tilde{u}}$	$\frac{\lvert\hat{v}\rvert}{U_\infty} \times 10^2$	$\theta_{\tilde{v}}$
1	8.4	180°	8.4	270°
2	6.0	180°	6.0	270°
3	3.9	180°	3.9	270°
I‡	2.9	180°	2.9	270°
5	1.6	180°	1.6	270°

‡ The run of Hsu *et al.* (1981) referred to as I.

TABLE 2. Amplitudes and the phase angles of $\tilde{u}$ and $\tilde{v}$ in the proximity of the interface

(1959) showed that to the first approximation the stream function is constant along $y^* =$ constant (see also Phillips 1977, p. 130). Hence we find

$$\tilde{u} = -ka(c-U)\,\mathrm{e}^{-ky^*}\cos(kx^*-\omega t), \tag{4.6a}$$

$$\tilde{v} = ka(c-U)\,\mathrm{e}^{-ky^*}\sin(kx^*-\omega t) \tag{4.6b}$$

as observed in the wave-following frame. The interface boundary condition is apparently satisfied by (4.6) for $\tilde{v}$, but not for $\tilde{u}$. This amplifies the significance of the surface orbital velocity and of the Stokes layer at the interface to the determination of $\tilde{u}$ outside the viscous sublayer. The predictions of $\tilde{u}$ and $\tilde{v}$ at $y^* = \delta_0$ obtained from (4.6) by taking the value of U at $y^* = \delta_0$ to be $U_0 + 10u_*$ are listed in table 2. We find the inviscid-model predictions agree reasonably well with the extrapolated values for $|\hat{v}|/U_\infty$. The systematically slightly lower values in the extrapolated results may be because the extrapolation neglected the curvature effect in the profiles of $|\hat{v}|/U_\infty$ shown in figure 4. It is interesting to observe that the extrapolated values of $\theta_{\tilde{u}}$ occur systematically between the interface-condition $\theta_{\tilde{u}} = 0°$ and the inviscid result $\theta_{\tilde{u}} = 180°$.

The inviscid approximation (4.6) does not provide a useful mechanism for the momentum transfer to the wave since (4.6) gives $-\overline{\tilde{u}\tilde{v}} = 0$. This is because the components of $\tilde{u}$ and $\tilde{v}$ that produce a non-zero correlation are neglected. These components are mainly produced owing to the existence of a critical layer near y_c^*. The profiles of $\tilde{u}$ and $\tilde{v}$ as shown in figures 3 and 4 are affected not only by the critical

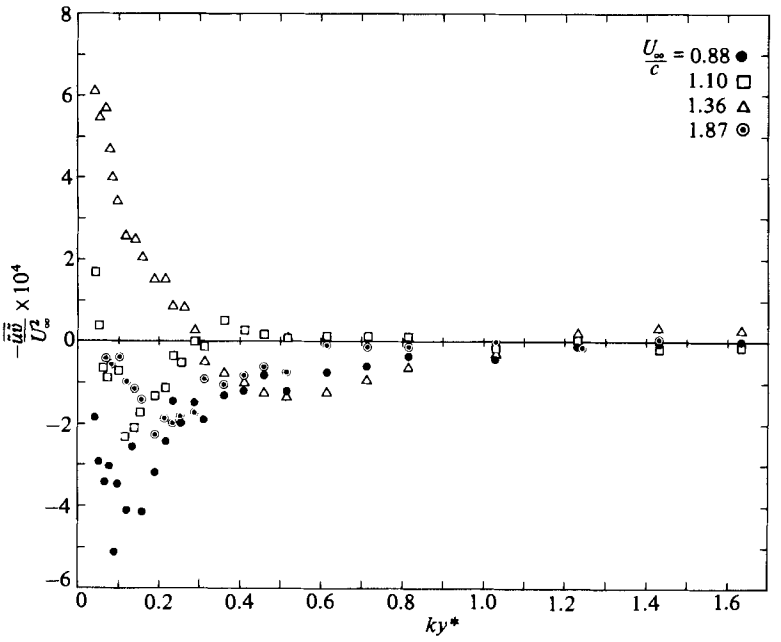

FIGURE 5. Profiles of the wave-associated Reynolds stress $-\overline{\tilde{u}\tilde{v}}$ as normalized by U_∞^2.

layer, but also by the turbulent mixing. When the critical height is high as in the cases of $U_\infty/c = 0.88$ and 1.10, the critical-layer effect is less significant than the turbulent mixing; the data of figures 3 and 4 seem to indicate that the turbulent mixing has little effect on the phase-angle distributions, although its effect on the amplitude of $\tilde{u}$ and $\tilde{v}$ is substantial. On the other hand, when the critical height is low as in the cases of $U_\infty/c = 1.36$ and 1.87, figures 3 and 4 seem to indicate that the critical-layer effect is significant and may become dominant over the effect of turbulent mixing. However, this does not imply that the turbulent mixing is insignificant. Turbulence may play an indirect but very important role in changing the structure of the critical layer since y_c^* is located in the very energetic turbulent region.

4.3.2. *Wave-associated Reynolds stress.* The distributions of the wave-associated Reynolds stress $-\overline{\tilde{u}\tilde{v}}(y^*)$ as normalized by U_∞^2 are presented in figure 5. It is more instructive to examine the profiles of $-\overline{\tilde{u}\tilde{v}}$ by decreasing ky^* from the free stream since this reveals how the wave-associated Reynolds stress is produced in the boundary layer. From figure 5, it is clear that most of the wave-associated Reynolds stress is produced near the interface, say, below $ky^* = 0.3$. We also find that, when $ky^* \to 0$, the values of $-\overline{\tilde{u}\tilde{v}}/U_\infty^2$ as shown in figure 5 tend to approach those at $y^* = \delta_0$ given in table 2. As the profiles shown in figure 5 contain the contributions not only from the fundamental mode but also from the harmonics, the above result seems to suggest that the contribution due to the harmonic components is negligible.

In figure 5, all the profiles indicate that $-\overline{\tilde{u}\tilde{v}}$ decreases to a negative minimum from an almost-zero value near the free stream, and then increases rapidly toward a positive value when $ky^* \to 0$. For $U_\infty/c = 0.88$ and 1.10 where the critical height is high, these minima occur below the critical height and approximately at $ky^* = 0.13$ and 0.10 respectively. On the other hand, when the critical height is low, they occur above the critical height and approximately at $ky^* = 0.54$, 0.35 and 0.20 for

$U_\infty/c = 1.36$, 1.54 and 1.87, respectively (see also figure 7 of I). When $U_\infty/c = 0.88$, the wave-induced flow is probably only affected by the viscous effect at the interface and the turbulent mixing in the boundary layer since the critical-layer effect is negligible. The Stokes layer at the interface due to viscous effects has a lengthscale characterized by $1/\beta$, where β is given by $\beta = (\omega/2\nu)^{\frac{1}{2}}$, if the turbulent effect is presumed to be negligible. For this study, $\beta = 0.443$ mm^{-1} and $k/\beta = 0.0091$. The existence of the Stokes layer results in the oscillatory behaviour in $\tilde{u}$ and $-\overline{\tilde{u}\tilde{v}}$. The maxima or the minima of $-\overline{\tilde{u}\tilde{v}}$ then occur at $\beta y^* = n\pi + \frac{1}{4}\pi$ depending on whether n are positive even or odd integers respectively, although these maxima and minima decrease rapidly with increasing y^*. This would imply that the first maximum is located at $ky^* = 0.0071$ and the first negative minimum is located at $ky^* = 0.036$. However, the upper portion of the Stokes layer is strongly affected by the turbulent mixing since the viscous sublayer of the mean flow is so thin. The simple eddy-viscosity model suggests that the turbulently modified Stokes layer may have a characteristic lengthscale based on $\beta_t = [\omega/2(\nu+\nu_t)]^{\frac{1}{2}}$, where $\nu_t = k_0 u_* y^*$ is the eddy viscosity. If to the first approximation the eddy mixing is assumed as a local process, the first maximum and negative minimum are then located at $\int_0^{y^*} \beta_t \, dy^* = \frac{1}{4}\pi$ and $\frac{5}{4}\pi$. Using $u_* = 0.043$ m/s for $U_\infty/c = 0.88$, we find these first maximum and negative minimum occur at $ky^* = 0.011$ and 0.12 respectively. It is interesting to see that the value of 0.12 agrees reasonably well with our observation of 0.13. Hence the effect of turbulence seems to diffuse the highly oscillatory nature of the viscous Stokes layer into the boundary layer through the turbulent mixing.

When the wind speed increases from $U_\infty/c = 0.88$ to 1.10, the critical height moves from $ky_c^* = \infty$ to 0.47. Flow below the critical height is slightly affected by the existence of the critical layer near y_c^*. The vertical diffusion of the viscous Stokes layer by turbulent mixing is compressed by the critical layer; hence the location where the first negative minimum occurs is lower than that of $U_\infty/c = 0.88$. In addition to this effect, the wave-associated Reynolds stress is produced in the critical layer as a result of the wind–wave interaction, as first demonstrated by Miles (1957). It is interesting to see that in figure 5 the wave-associated Reynolds stress for $U_\infty/c = 1.10$ below the critical layer is higher than that for $U_\infty/c = 0.88$ by an almost constant amount of 2.8 as estimated in table 2(*b*). This seems to be consistent with Miles' (1957) theory. In other words, our observed $-\overline{\tilde{u}\tilde{v}}$ shown in figure 5 for $U_\infty/c = 1.10$ seems to behave as the additive results of the wave-associated Reynolds stresses due to the turbulently diffused Stokes layer and the critical layer.

When the wind is so high that the critical layer is located at the lower portion of the turbulent boundary layer and near the interface, the wave-associated Reynolds stress below the critical layer as produced by the critical layer is large; this implies the existence of a component in $\tilde{u}$ which is very large and is 180° different in phase from $\tilde{v}$. This amplifies the significance of the wave nonlinear effect in the critical layer since the location of the critical height is greatly modified by $\tilde{u}$. The flowfield between the Stokes layer and the critical layer is very complicated as these two layers are so close to each other; however, the flowfield above the critical layer is now over most portions of the turbulent boundary layer and becomes somehow more similar to a turbulent flow over a stationary wavy solid boundary. It should be noted that the flow over a solid wavy boundary represents the case of $U_\infty/c = \infty$ and $ky_c^* = 0$. Under this extreme situation, the critical layer attached at the wavy boundary is very thin in comparison with the amplitude of the waveform. Hence the streamlines above the critical layer are expected to bend over along the wavy solid boundary. The inviscid theory then suggests that $\theta_{\tilde{u}} = 0°$ and $\theta_{\tilde{v}} = 90°$ as inferred from (4.6), where c is set

to be zero. When c is positive and non-zero as for water waves, the critical height y_c^* is located above the interface depending on U_∞/c. The magnitudes of $\tilde{u}$ and $\tilde{v}$ near the free stream are probably scaled with $U_\infty - c$, but the phase of $\tilde{u}$ and $\tilde{v}$ may depend on the upper boundary of the cat's-eye pattern. The undulation of this upper boundary is the combined result of the undulations of the critical layer (cat's-eye displacement) and of the critical height ($y_c^* =$ constant). The fact that the cat's-eye is located in the lee of the wave near the trough tends to shift $\theta_{\tilde{v}}$ near the free stream from 90° to 270°, and simultaneously $\theta_{\tilde{u}}$ from 0° to 180° in the downstream direction, as c increases from zero. These are indicated by the observed $\tilde{u}$ and $\tilde{v}$ shown in figures 3 and 4. The effect of the critical layer is to redistribute the mean vorticity field near the critical height so that the flowfields below and above the critical layer can have a smooth transition. As the critical height is located in the energetic turbulent region, the critical layer is probably very diffusive, very thick and highly nonlinear. Since when U_∞/c is large the critical height is low, the contraction of the cat's-eye on the flowfield below the critical layer is very strong. A component of $\tilde{u}$ in phase with the wave slope as a result of this contraction then may become dominant in $\tilde{u}$ near the interface. This may lead to the observed $\theta_{\tilde{u}}$ near the interface as shown in figure 3 for $U_\infty/c = 1.36$ and 1.87. The distributions of $\theta_{\tilde{u}}$ and $\theta_{\tilde{v}}$ are then consequences of the smooth transition from the values near the interface to those near the free stream by the critical layer. As a result, the value of $-\overline{\tilde{u}\tilde{v}}$ has a positive maximum near the interface, but outside the viscous sublayer and decreases to a negative minimum at the height where $\theta_{\tilde{u}} \approx \theta_{\tilde{v}}$, and then approaches zero when ky^* aproaches the free stream. It should be noted that the location of the negative minimum for the case of $U_\infty/c = 1.36$ and 1.87 is scaled with the critical height y_c^*. Hence when U_∞/c increases, the location of minimum $-\overline{\tilde{u}\tilde{v}}$ moves toward the interface.

4.3.3. *Wave-induced turbulent Reynolds stresses.* The perturbation of the wind turbulent Reynolds stresses by the wave is described by $\tilde{r}_{ij}$, which from (2.3) is defined as

$$\tilde{r}_{ij} = \langle u_i' u_j' \rangle - \overline{u_i' u_j'}. \tag{4.7}$$

The scheme used to reduce $\tilde{r}_{ij}$ was described in I. The profiles for the amplitude $|\hat{r}_{ij}|$ and the phase angle $\theta_{\tilde{r}_{ij}}$ are shown in figures 6, 7 and 8 for $\tilde{r}_{11}$, $\tilde{r}_{12}$ and $\tilde{r}_{22}$ respectively. The phase jump of 180° at $ky^* = 0.5$ when $U_\infty/c = 1.87$ resembles that observed earlier in I; however, when $U_\infty/c = 0.88$, 1.10 and 1.36, the results of $\theta_{\tilde{r}_{ij}}$ shown in figures 6–8 do not reveal any phase jump of 180°. As mentioned in I, the phase jump implies that the wave-induced turbulent Reynolds stresses at the phase jump location are equal to zero. The oscillatory stresses above and below the phase jump location are exerted in the opposite directions. From figures 6–8, it is clear that the distributions of $\theta_{\tilde{r}_{ij}}$ are very sensitive to the parameter U_∞/c except those in the close proximity of the interface, where we find that $\theta_{\tilde{r}_{11}} \to 0°$, $\theta_{\tilde{r}_{12}} \to 90°$ and $\theta_{\tilde{r}_{22}} \to 0°$ when $ky^* \to 0$ for all U_∞/c. The behaviour of these limit values of $\theta_{\tilde{r}_{ij}}$ when $ky^* \to 0$ bears some significance in the interface physics which is discussed later. On the other hand, the distributions of $|\hat{r}_{ij}|$ as shown in figures 6–8 seems only to suggest that the amplitudes of $\tilde{r}_{ij}$ are scaled with the intensity of the mean turbulent flowfield, which is large near the interface and decays to zero near the free stream.

It is clear that most of the distinguished features of the wave-induced turbulent Reynolds stresses are demonstrated by the phase distributions $\theta_{\tilde{r}_{ij}}$, from which a general structure for $\tilde{r}_{ij}$ emerges. It is more instructive to examine the structure of $\tilde{r}_{ij}$ by observing the flow in a frame moving with the wave celerity, i.e. $x_c^* = x^* - ct$,

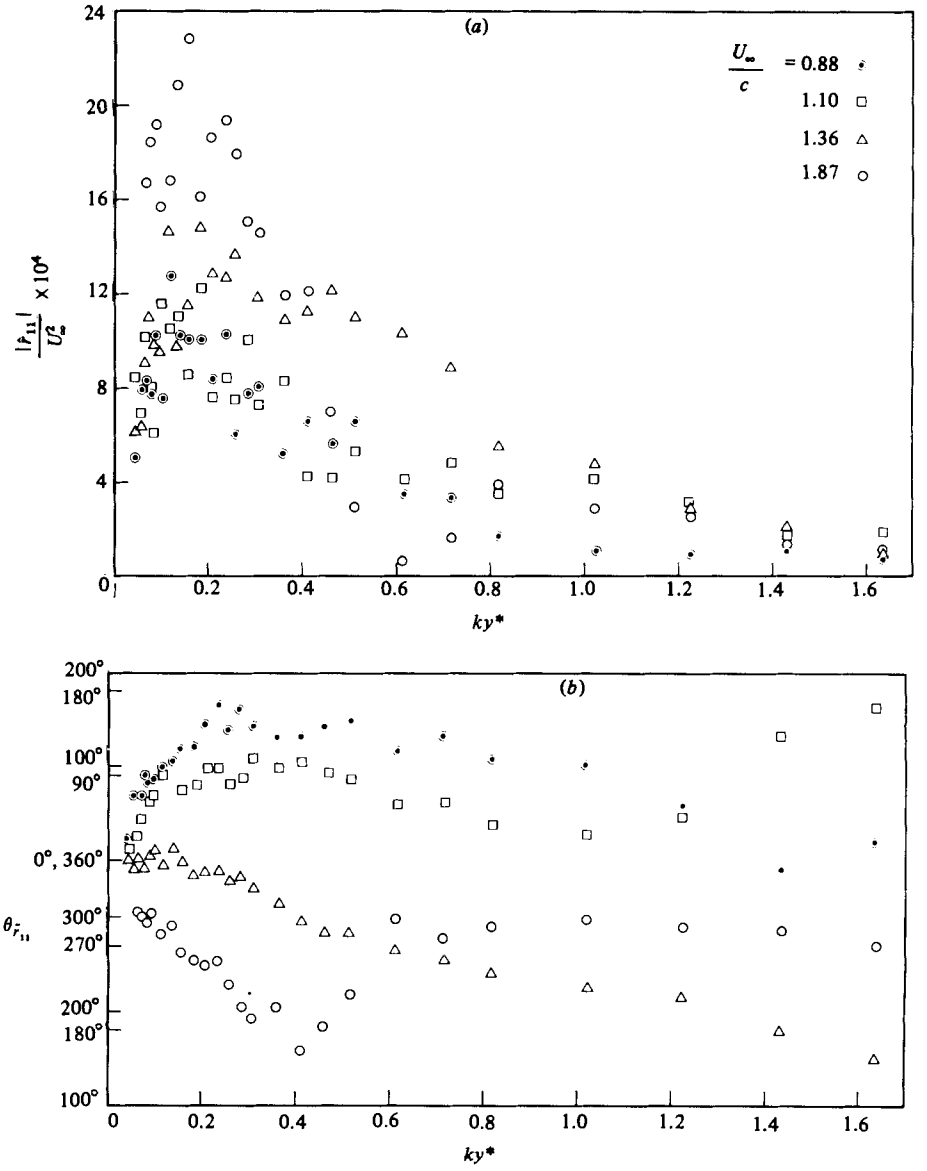

FIGURE 6. Profiles of the wave-induced turbulent Reynolds stress $\tilde{r}_{11}$: (*a*) amplitudes; (*b*) phases.

and by considering the advection of the wave-induced turbulent perturbations in this new frame. We imagine first a turbulent wind over a flat water surface, and then introduce the mechanically generated water wave. The wave action in producing the wave-induced turbulent Reynolds stresses as a result of contraction on the turbulent flowfield commences first in the very proximity of the interface. This wave action is relaxed when it penetrates the turbulent boundary layer and then reaches a steady state as observed in the x_c^* frame. In the proximity of the interface, the wave-induced turbulent Reynolds stresses are solely dependent on the intensity of the mean turbulent field and on the undulation of the surface wave, but not on the parameter U_∞/c.

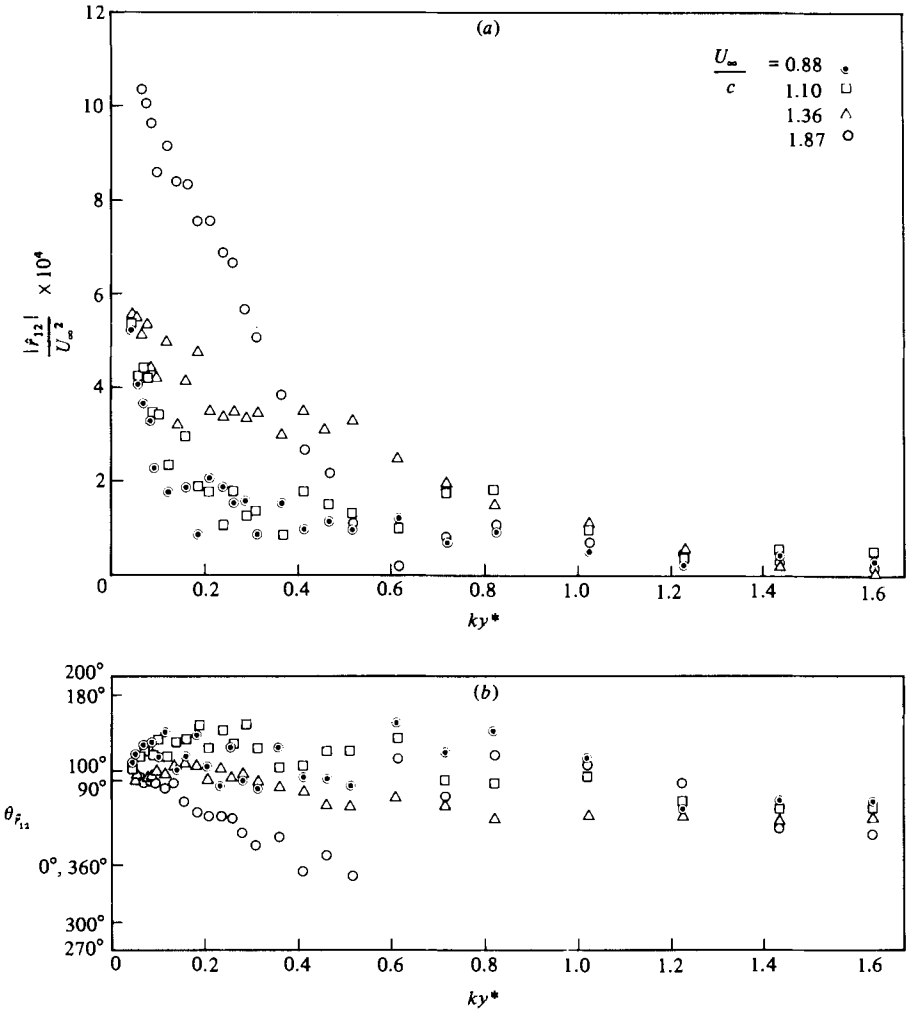

FIGURE 7. Profiles of the wave-induced turbulent Reynolds stress $\tilde{r}_{12}$: (*a*) amplitudes; (*b*) phases.

To delineate this dependence, let us begin with flows of no turbulence. If $\tilde{h}(x^*, y^*, t)$ is the vertical displacement of the mean streamlines induced by the surface wave motion, the condition of no flow across a streamline requires

$$\langle v \rangle = \frac{\partial \tilde{h}}{\partial t^*} + \langle u \rangle \frac{\partial \tilde{h}}{\partial x^*}. \tag{4.8}$$

When the turbulence is introduced, there is an active component $\tilde{v}'$ in v' (see Davis 1974) which describes the coupling between the wave and the turbulence. To the first approximation, this active component $\tilde{v}'$ can be obtained by perturbing the right-hand side of (4.8) with turbulent fluctuations u' and h'. This leads to

$$\tilde{v}' = u' \frac{\partial \tilde{h}}{\partial x^*} + \tilde{u} \frac{\partial h'}{\partial x^*}. \tag{4.9}$$

(We derive this concept from Miles (1967), but here we include the component h' to

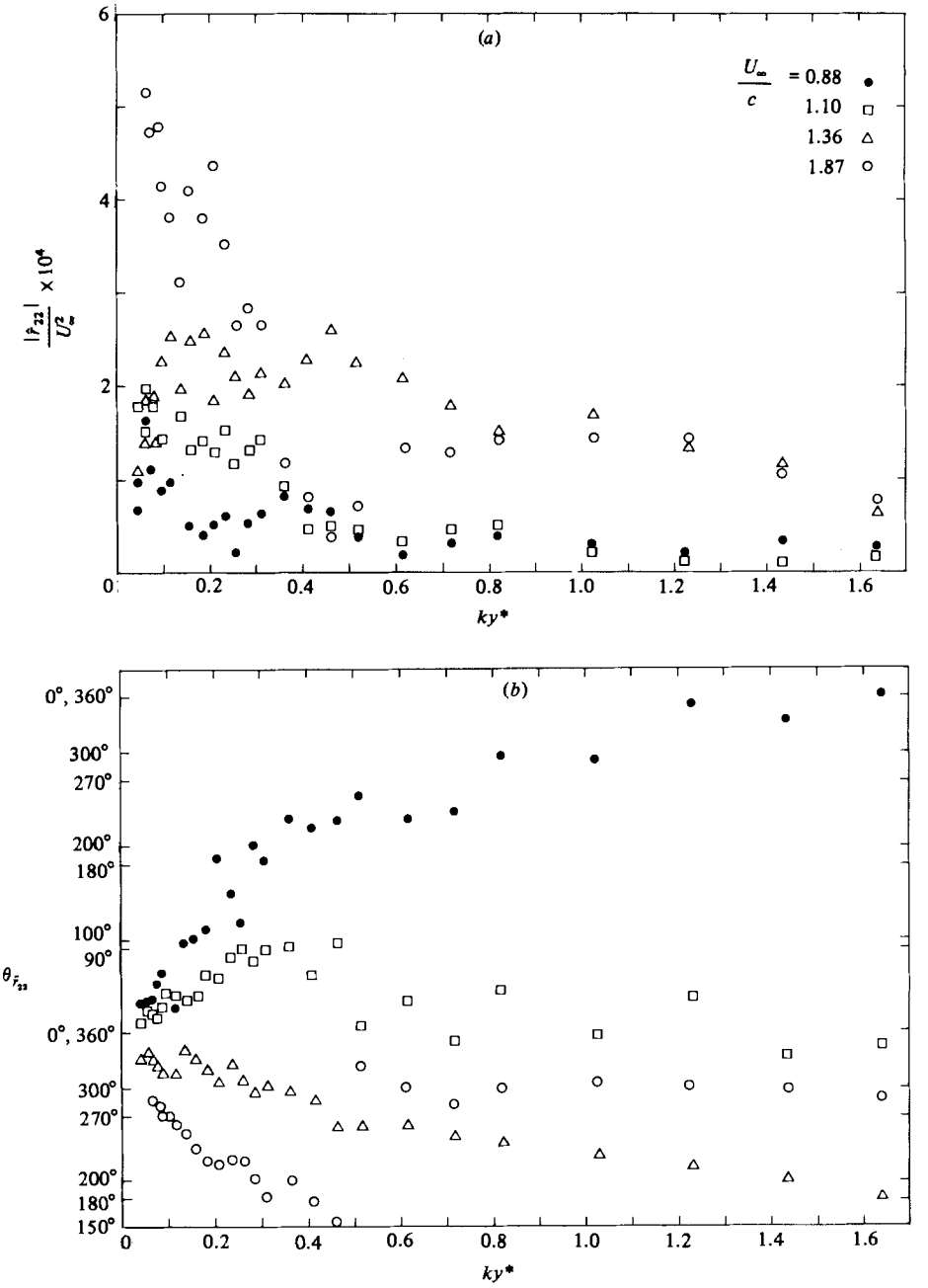

FIGURE 8. Profiles of the wave-induced turbulent Reynolds stress $\tilde{r}_{22}$: (*a*) amplitudes; (*b*) phases.

capture the actual flow characteristics better.) The active component $\tilde{u}'$ in u' is related to $\tilde{v}'$ through the perturbed continuity equation in (x^*, y^*, z^*), i.e.

$$\frac{\partial \tilde{u}'}{\partial x^*} - f\frac{\partial \tilde{\eta}}{\partial x^*}\frac{\partial u'}{\partial y^*} + \frac{\partial u'}{\partial x^*}\frac{\partial f}{\partial y^*}\tilde{\eta} + \frac{\partial \tilde{v}'}{\partial y^*} = 0. \tag{4.10}$$

The solution to $\tilde{u}'$ by substituting (4.9) into (4.10) cannot be obtained exactly, since

$\tilde{h}$ is not known *a priori*. However, when $ky^* \to 0$ we can assume that $\tilde{h} = f\tilde{\eta}$ (which is true from the interface boundary condition and from the inviscid theory) and that the lengthscale of turbulence is very small compared with the wavelength of a surface wave (which is true near the interface because the lengthscale of turbulence there is proportional to y^*), so that to first order $\tilde{u}'$ is found to be

$$\tilde{u} = -u' \frac{\partial f}{\partial y^*} \tilde{\eta} - \tilde{u} \frac{\partial h'}{\partial y^*} - h' \frac{\partial \tilde{u}}{\partial y^*}. \tag{4.11}$$

The wave-induced turbulent Reynolds stresses $\tilde{r}_{ij}$ in terms of $\tilde{u}'$ and $\tilde{v}'$ are (following Davis 1974)

$$\tilde{r}_{ij}(x^*, y^*, t) = \langle \tilde{u}_i' u_j' \rangle + \langle \tilde{u}_j' u_i' \rangle, \tag{4.12}$$

where $\tilde{u}_i' = (\tilde{u}', \tilde{v}')$ and $u_i' = (u', v')$. The substitution of (4.9) and (4.11) into (4.12) yields explicitly

$$\tilde{r}_{11} = -2\overline{u'u'} \frac{\partial f}{\partial y^*} \tilde{\eta} - 2\overline{u' \frac{\partial h'}{\partial y^*}} \tilde{u} - 2\overline{u'h'} \frac{\partial \tilde{u}}{\partial y^*}, \tag{4.13a}$$

$$\tilde{r}_{12} = \overline{u'u'} f \frac{\partial \tilde{\eta}}{\partial x^*} + \overline{u' \frac{\partial h'}{\partial x^*}} \tilde{u} - \overline{u'v'} \frac{\partial f}{\partial y^*} \tilde{\eta} - \overline{v' \frac{\partial h'}{\partial y^*}} \tilde{u} - \overline{v'h'} \frac{\partial \tilde{u}}{\partial y^*}, \tag{4.13b}$$

$$\tilde{r}_{22} = 2\overline{u'v'} f \frac{\partial \tilde{\eta}}{\partial x^*} + 2\overline{v' \frac{\partial h'}{\partial x^*}} \tilde{u}. \tag{4.13c}$$

In (4.13) the correlations of h' and its derivatives with u_i' remain to be determined from the characteristics of the turbulence. The detail of them is provided in a subsequent paper when the closure modelling of $\tilde{r}_{ij}$ and the predictions of the wave-induced flow are presented. However, it will suffice here to note that, when $ky^* \to 0$, the first terms on the right-hand side of (4.13*a*, *b*) become the dominant terms because $\overline{u'u'} \gg -\overline{u'v'} \approx \overline{v'v'}$. Thus suggests that when $Ky^* \to 0$ we shall have $\tilde{r}_{11} \approx 2\overline{u'u'}\, k\tilde{\eta}$ and $\tilde{r}_{12} \approx \overline{u'u'}\, \partial\tilde{\eta}/\partial x^*$, i.e. $|\hat{r}_{11}| \approx 2\overline{u'v'}\, ka$, $\theta_{\tilde{r}_{11}} \approx 0°$, $|\hat{r}_{12}| \approx \overline{u'u'}\, ka \approx \frac{1}{2}|\hat{r}_{11}|$ and $\theta_{\tilde{r}_{12}} \approx 90°$. The measured $\overline{u'u'}/U_\infty^2$ in this study is about $(50\text{–}70) \times 10^{-4}$; hence, we shall expect $|\hat{r}_{11}|/U_\infty^2 \approx (10\text{–}14) \times 10^{-4}$ and $|\hat{r}_{12}|/U_\infty^2 \approx (5\text{–}7) \times 10^{-4}$. Our observations of $\tilde{r}_{ij}$ as shown in figures 6 and 7 apparently confirm the above predictions.

The above derivations indicate that, in the close proximity of the interface, the maxima of the wave action are located at a fixed phase relative to the surface wave. The wave-induced turbulent intensity is mainly produced by compression and stretching of the turbulent flowfield by surface undulation so the maximum intensity occurs above the crests; on the other hand, the wave-induced shear stress $\tilde{r}_{12}$ is produced by the change in the direction of u' by surface undulation so the maximum $\tilde{r}_{12}$ occurs when the wave slope is maximum. When the wave action penetrates the turbulent boundary layer, these maxima to the first approximation are advected by the mean velocity $U-c$. When $U_\infty/c = 0.88$ and 1.10, the boundary layer is mainly below the critical height and $U-c$ there is negative; the advection then tends to shift the phase of the wave action into the upstream direction. On the other hand, when $U_\infty/c = 1.36$ and 1.87, most of the turbulent boundary layer is above the critical height and $U-c$ there is positive; the phase of the wave action is then shifted into the downstream direction during its relaxation. For consistence, the phase of $\tilde{r}_{ij}$ as shown in figures 6–8 for $U_\infty/c = 1.87$ and $ky^* > 0.5$ are shifted by 180°, while the amplitudes there are interpreted as negative so that both the amplitude and the phase are continuous and smoothly varying at $ky^* = 0.5$.

In fact, the above wave-action relaxation process is closely related to the response

of turbulence to a varying mean flow. It is well known that the turbulent intensity is decreased in an accelerating mean flow. The turbulent boundary-layer flow over water surface waves as observed in x_c^* is regarded as the flow over a series of convergent and divergent regions undergoing acceleration and deceleration processes. When ky_c^* is large, the mean flow is in the $-x_c^*$ direction, so that the deceleration process occurs in the windward region (phase-lag angle from 0° to 180°). Consequently, the turbulent intensity $\langle u_i' u_i' \rangle$ (which is insensitive to the mean-flow direction) is maximum there. As a result, the shear stress $-\langle(-u')v'\rangle$ acting in the $-x_c^*$ direction is also maximum there since higher turbulent intensity implies higher shear stress. This is equivalent to the condition that $\langle u'v' \rangle$ has the maximum in the windward region. Our observed phases of $\tilde{r}_{11}$, $\tilde{r}_{12}$ and $\tilde{r}_{22}$ for $U_\infty/c = 0.88$ and 1.10 apparently agree very well with the above arguments.

When ky_c^* is very low, the mean flow is in the x_c^* direction, so that the deceleration process occurs in the leeward region (phase-lag angle from 180° to 360°). Consequently, the turbulent intensity $\langle u_i' u_i' \rangle$ and the shear stress $-\langle u'v' \rangle$ are maximal in the leeward. Hence, $\langle u'v' \rangle$ is maximal in the windward. These are confirmed by our observations of $\tilde{r}_{ij}$ for the cases of $U_\infty/c = 1.36$, 1.54 and 1.87. The phase jump of 180° for the cases of $U_\infty/c = 1.54$ and 1.87 then becomes a necessity in order to guarantee that the maximum turbulent intensity and the shear stress occur in the leeward. The phase jump occurs when the phases of $\tilde{r}_{11}$ and $\tilde{r}_{22}$ are 180° and when the phase of $\tilde{r}_{12}$ is 0°.

The most significant results of $\tilde{r}_{ij}$ as indicated by figures 6–8 are their pertinent relationship to the wave-induced velocities. The comparisons between the phase distributions of the wave-induced velocities and the wave-induced turbulent Reynolds stresses indicate that the eddy-viscosity-type relation found in I for $U_\infty/c = 1.54$ now seems to hold for the other U_∞/c values of this study. This would imply that the relaxation of the wave action in the turbulent boundary layer is governed not only by the advection, but also by the turbulent eddy mixing. The eddy-viscosity-type relation between $\tilde{u}_i$ and $\tilde{r}_{ij}$ is of great significance – its details were examined by Hsu, Hsu & Street (1977).

It is worth noting that the structure of the wave-induced turbulent Reynolds stresses as observed in this study is very similar to the modal structure of an eigenvalue problem usually encountered in hydrodynamic stability theory, because $\tilde{r}_{ij}$ at $ky^* = 0$ and ∞ are required to be zero as necessary boundary conditions. While when $U_\infty/c = 0.88$, 1.10 and 1.36 the distribution of $\tilde{r}_{ij}$ along ky^* is dominated by the first eigenmode, it is dominated by the second eigenmode when $U_\infty/c = 1.54$ and 1.87, i.e. the amplitudes of $\tilde{r}_{ij}$ change sign in the boundary layer if the phases of $\tilde{r}_{ij}$ are regarded as continuous.

5. Structure of wave-induced flowfields

In §4 we have discussed the behaviour of the wave-induced velocities and the wave-induced turbulent Reynolds stresses based on the data obtained in this study. Here we attempt to give a more concise but more systematic description of the wave-induced flowfields using the characteristic scales of the wave, the wind and of their coupling. In order to do this, we need to start with the case of zero wind to explore the basic scales of the wave-perturbed flowfields and to show the structure of the Stokes layer under laminar conditions. Then the wind is introduced, but the wind speed is still within the range of $U_\infty < c$. The characteristic scales of the turbulent wind are discussed. The case of $U_\infty < c$ represents the simplest first-step

coupling between the wind and the wave because the critical height is regarded as at $ky_c^* = \infty$, i.e. the critical layer does not play any significant role in describing the wave-induced flowfields. The effect of the mean wind and of the turbulence on the wave-induced flow as well as on the Stokes layer under this simplest coupling condition are discussed. Finally, the wind speed is further increased to the range of $U_\infty > c$ to produce a critical layer. The lengthscales of the critical height and of the critical layer are discussed. The effect of the critical layer on the wave-induced flowfields in relation to the energy transfer from wind to wave, the changes in the critical-layer structure as influenced by nonlinear process and by turbulent mixing, and the interaction between the critical layer and the Stokes layer are examined. The discussions given in this section are for an infinitely extended airflow, which are expected also to be applicable to the results of this experiment since $kH = 4.0$, where H is the channel-roof height of this experiment.

5.1. *Wave perturbations in quiescent air*

When there is no wind, the inviscid solution for the wave-induced velocities is given by

$$\tilde{u} = -kac\,\mathrm{e}^{-ky^*}\cos(kx^* - \omega t), \tag{5.1a}$$

$$\tilde{v} = kac\,\mathrm{e}^{-ky^*}\sin(kx^* - \omega t). \tag{5.1b}$$

Equation (5.1a) does not satisfy the interface boundary condition, which is given by $\tilde{u}(x^*, 0, t) = kac\cos(kx^* - \omega t)$ according to the orbital velocity of the surface wave. Hence, the viscous effect is significant in the proximity of the interface. The viscous effect results in a Stokes layer near the interface and the solutions to the wave-induced velocities are modified to

$$\tilde{u} = -kac\,\mathrm{e}^{-ky^*}\cos(kx^* - \omega t) + 2kac\,\mathrm{e}^{-\beta y^*}\cos(kx^* - \omega t + \beta y^*), \tag{5.2a}$$

$$\tilde{v} = kac\,\mathrm{e}^{-ky^*}\sin(kx^* - \omega t) - 2^{\frac{1}{2}}kac\left(\frac{k}{\beta}\right)[\mathrm{e}^{-\beta y^*}\cos(kx^* - \omega t + \beta y^* - \tfrac{1}{4}\pi) - \cos(kx^* - \omega t - \tfrac{1}{4}\pi)], \tag{5.2b}$$

where $\beta = (\omega/2\nu)^{\frac{1}{2}}$ is the reciprocal of the Stokes-layer thickness (Phillips 1977, p. 45). From (5.2), it is clear that the change in $\tilde{u}$ by the viscous effect is drastic, but that in $\tilde{v}$ is only slight because k/β is small. For this experiment $k/\beta = 0.0091$. The magnitude of $-\overline{\tilde{u}\tilde{v}}$ then is oscillatory along y^* and to the first approximation is given by

$$-\overline{\tilde{u}\tilde{v}} = (kac)^2\,\mathrm{e}^{-(k+\beta)\,y^*}\sin\beta y^*, \tag{5.3}$$

which has maxima and minima at $\beta y^* = n\pi + \frac{1}{4}\pi$, as mentioned in §4.3.2.

It is clear that for this quiescent-air case the wave-induced flow is characterized by three lengthscales, i.e. the wavelength k^{-1}, the wave amplitude a and the Stokes-layer thickness β^{-1}. The wavelength is a global scale which characterizes the extent of the wave-induced flowfield; the wave amplitude and the Stokes-layer thickness are local scales which characterize the undulation as well as the variation of the wave-induced flowfield near the interface. Because $k/\beta \ll ka$ for this study, the Stokes layer is a very thin layer undulating along the wave surface.

5.2. *Wave perturbations in light wind* ($U_\infty < c$)

When a turbulent wind is introduced, the wave perturbations as described in §5.1 are strongly affected by the mean and the turbulent velocities. The wind flowfield has a global scale of the boundary-layer thickness δ, which characterizes the extent

of mean-velocity variation and turbulent mixing, and a local scale of the viscous-sublayer thickness δ_0 ($= 10\nu/u_*$), which characterizes the wind shear and the lower limit of turbulent mixing near the interface. The coupling between the wind and the wave depends not only on the parameters formed by the lengthscales of the wind and the waves, but also by the parameter U_∞/c, which determines the critical height and the critical-layer thickness. For this study, $k\delta \approx 1.0$; hence the wave-induced flow is expected to be affected by the wind profile. From the values of $k\delta_0$ given in table 1, we also expect that the upper portion of the Stokes layer is affected strongly by turbulent mixing. In this subsection, we discuss only the case of $U_\infty < c$, i.e. when the critical height is very large so that the effect of the critical layer is negligible.

We first consider the effect of the mean wind and then attempt to examine the influence of turbulent mixing. When the effect of turbulence is ignored, the analysis is quasi-laminar. The inviscid solution to the wave-induced velocities to the first approximation, according to Miles (1957), is given by (4.6), which appears to be a multiplication of (5.1) by a factor of $1 - U/c$. Hence the mean wind velocity under the situation of $U_\infty < c$ tends to cause the wave-induced flowfields to decay much faster in the boundary layer. On the other hand, the viscous friction-layer solution at the interface, according to the analyses of Benjamin (1959), is expressible in terms of Airy functions, which is a result of the modification of the Stokes layer by the mean shear of the wind profile at the interface. The effect of the surface wind shear on the Stokes layer is quantified by the Tietjens function $D(-Z_0)$ defined conventionally in hydrodynamic stability theory (Lin 1955). The argument Z_0 defined by $(kU_0'/\nu)^{\frac{1}{3}} c/U_0'$, where U_0' is $\mathrm{d}U/\mathrm{d}y^*$ at $y^* = 0$, is the parameter that measures this mean shear effect. For aerodynamically smooth turbulent-velocity profiles, $U_0' = u_*^2/\nu$. Hence, the parameter Z_0 can be expressed as

$$Z_0 = \left(\frac{c}{u_*}\right)^{\frac{4}{3}} R_{\mathrm{w}}^{-\frac{1}{3}}, \tag{5.4}$$

where $R_{\mathrm{w}} = c/k\nu = 2(\beta/k)^2$ is the wave Reynolds number. In fact, the surface friction layer behaves as if there were virtually a critical layer with thickness of order $(kU_0'/\nu)^{-\frac{1}{3}}$ located at $y^* = c/U_0'$. The parameter Z_0 then denotes the distance of the interface from this virtual critical layer, using the critical-layer thickness as a measure. It should be noted that the actual critical layer may be located much higher than c/U_0', or even may not exist. We also noted that the surface friction layer will reduce asymptotically to the Stokes layer if $Z_0 \to \infty$. For this reason, we shall refer to this surface friction layer as a 'modified' Stokes layer. The modified Stokes layer has a thickness of order β^{-1} if Z_0 is very large and of order $(kU_0'/\nu)^{-\frac{1}{3}}$ if Z_0 is small. For better understanding of the conditions of this experiment, the values of kc/U_0', $k(kU_0'/\nu)^{-\frac{1}{3}}$ and Z_0 are listed in table 3. Since Z_0 shown in table 3 is not very large (say greater than 8 as cited by Benjamin 1959), the effect of the surface mean shear on the Stokes layer is considerable. However, as shown by Benjamin, this does not provide any significant mechanism for the energy transfer from wind to wave.

We now examine the effect of turbulence on the wave-induced flow. Intuitively, the diffusion due to turbulent mixing is expected to make the inviscid wave-induced velocity profiles given by (4.6) have a more uniform distribution in the boundary layer with a more rapid change near the interface. The quasi-laminar analysis using the logarithmic mean-velocity profile U rather than a laminar profile provides the first account of this mixing effect. Further account of this effect requires the inclusion of the wave-induced turbulent Reynolds stresses in the wave-perturbation equations. The first test ground for the closure modelling of the wave-induced turbulent

Run	kc/U_0'	$k(\nu/kU_0')^{\frac{1}{3}}$	Z_0	$k\delta_c$	Z_c	$k\delta_{ct}$	Z_{ct}	A_∞	$k\delta_m$	Z_m	$\frac{\lvert\hat{v}\rvert_c}{U_\infty}\times 10^2$	$\frac{-\overline{\tilde{u}\tilde{v}}}{U_\infty^2}\times 10^4$	Γ
1	0.054	0.013	4.1	—	∞	—	∞	—	—	∞	—	—	—
2	0.032	0.011	2.9	0.060	7.8	0.33	1.4	2.0	0.47	1.0	0.95	3.0	2.1
3	0.019	0.0092	2.1	0.031	2.7	0.11	0.81	1.8	0.16	0.53	0.72	9.6	2.0
I‡	0.014	0.0083	1.7	0.022	1.5	0.057	0.60	1.1	0.075	0.45	0.35	5.7	1.3
4	0.0083	0.0070	1.2	0.014	0.86	0.028	0.43	0.55	0.026	0.45	0.12	1.9	0.60

‡ The run of Hsu *et al.* (1981) referred to as I.

TABLE 3. Local lengthscales associated with the dynamic coupling between the wind and the wave

Reynolds stresses should probably be on the condition of $U_\infty < c$, since the flow is not complicated by the existence of a critical layer. However, in view of our observations of $\tilde{u}_t$ and $\tilde{r}_{ij}$ shown in §4, a simple eddy-viscosity model may be able to provide reasonable results.

The effect of turbulence on the modified Stokes layer is more subtle, partially because there are no data available for this layer. The comparisons of the values of kc/U_0' and $k(kU_0'/\nu)^{-\frac{1}{3}}$ shown in table 3 with the values of $k\delta_0$ shown in table 1 indicate that the upper portion of the modified Stokes layer is strongly influenced by turbulence. The turbulent diffusion tends to make the Stokes layer penetrate deeper into the boundary layer. The value of β then can probably be replaced by $\beta_t = [\omega/2(\nu+\nu_t)]^{\frac{1}{2}}$. Equation (5.3) for $-\overline{\tilde{u}\tilde{v}}$ for the case of $U_\infty < c$ may be modified into

$$-\overline{\tilde{u}\tilde{v}} = A_0(kac)^2 \exp\left(-ky^* + \int_0^{y^*} \beta_t \mathrm{d}y^*\right) \sin\left(\int_0^{y^*} \beta_t \mathrm{d}y^*\right), \tag{5.5}$$

where A_0 is an amplification factor accounting for the effect of the mean flow.† For $U_\infty/c = 0.88$, we find from (5.5) that the first negative minimum of $-\overline{\tilde{u}\tilde{v}}$ occurs at $ky^* = 0.12$, as mentioned in §4.3.2, and the corresponding value of $-\overline{\tilde{u}\tilde{v}}/U_\infty^2$ there is -4.5×10^{-4} if we take $A_0 = 1.5$. It is noted that the relevant parameter for the effect of turbulence on the Stokes layer is $R_w^{-\frac{1}{2}}(c/u_*)$, which measures the thickness of the viscous sublayer relative to the Stokes layer, i.e. the extent of the upper portion being affected by turbulent diffusion.

5.3. *Wave perturbations in large wind* ($U_\infty > c$)

When $U_\infty > c$, there is a critical height where $U(y_c^*) = c$. In the moving frame x_c^*, where the waveform at the interface is steady, the flow above y_c^* moves downstream, while that below y_c^* and above the interface moves upstream because the mean velocity is presumed to increase monotonically. This leads to the existence of a critical layer at y_c^* to smooth the discontinuity in the flow vorticity at y_c^*. The extent of the critical layer in affecting the wave-induced flow then depends on the structure of the critical layer. Since y_c^* measures the location of the critical layer in the turbulent boundary layer, one's first intuition is to regard it as a global scale. On the other hand, the critical-layer thickness is then regarded as a local scale. Both lengthscales are dependent on the dynamic coupling parameter U_∞/c.

For an aerodynamically smooth mean-velocity profile as encountered in this study, the critical height located in the logarithmic region is determined by

$$y_c^* = \frac{\nu}{u_*} \exp\left[k_0\left(\frac{c}{u_*} - C\right)\right]. \tag{5.6}$$

Equation (5.6) indicates that the critical height decreases exponentially with decreasing c/u_*. Hence the regime below the critical layer shrinks rapidly from the one comparable to the boundary-layer thickness when $U_\infty \approx c$ to that comparable to the viscous-sublayer thickness when $U_\infty \approx 2c$. This is indicated by the values of $k\delta_0$ and ky_c^* shown in table 1. The wave-induced flows then are of different characteristics when y_c^* is comparable to the global scale (the case of $U_\infty/c = 1.10$) and when y_c^* is comparable to the local scale (the cases of $U_\infty/c = 1.36$ and 1.87). Before we discuss these two different flow characteristics, we shall examine the lengthscale of the critical layer.

† Davis (see his appendix to this paper) has extended our result and provided a more detailed analysis of the turbulent Stokes layer, based on the eddy-viscosity model.

The existence of the critical layer is to smooth the discontinuity that occurs at y_c^* in an inviscid quasi-laminar linear analysis. The viscous effect is significant near y_c^* if we presume no turbulent mixing and that the wave perturbation is linear. According to Miles (1959), the thickness of the critical layer as produced by viscous effects is given by

$$\delta_c = \left(\frac{\nu}{kU_c'}\right)^{\frac{1}{3}}, \tag{5.7}$$

where U_c' is the value of $\mathrm{d}U/\mathrm{d}y^*$ at y_c^*. The values of $k\delta_c$ for this study and I are listed in table 3; they are small compared with the boundary-layer thickness. The effect on the viscous critical layer due to the existence of the interface is measured by the parameter Z_c defined as y_c^*/δ_c; the values of Z_c are also listed in table 3. As discussed earlier for the mean-flow shearing effect on the Stokes layer, we expect that the effect of the interface on the viscous critical layer is negligible if Z_c is larger than 8. However, the role of viscous diffusion may be taken by turbulent mixing since the critical height is in the energetic turbulent region. The thickness of the turbulently modified critical layer, say δ_{ct}, under the linear analysis may still be given by (5.7), except that ν is now replaced by the eddy viscosity $\nu_t = k_0 u_* y^*$ at y_c^*. The values of $k\delta_{ct}$ for this study are given in table 3, together with the values of $Z_{ct} = y_c^*/\delta_{ct}$. Apparently, the turbulent critical layer is much thicker than the viscous critical layer and in the case of $U_\infty/c = 1.10$ even becomes comparable to the boundary layer. The compression of the flow below the turbulent critical layer due to the interface is substantial, especially when $U_\infty/c = 1.87$.

It was Davis (1969) and Benney & Bergeron (1969) who showed that the nonlinear convection due to the wave-perturbed flow can have a role in smoothing the vorticity discontinuity at y_c^*. The significance of this nonlinear effect in determining the wave-induced flowfield, as well as in enhancing the energy transfer from wind to wave, was emphasized by Robinson (1974) and Phillips (1977). The theory of the nonlinear critical layer resembles nonlinear hydrodynamic stability theory. According to Phillips (1977, p. 122), the thickness of the nonlinear critical layer is given by

$$\delta_m = \left(\frac{4|\hat{v}|_c}{kU_c'}\right)^{\frac{1}{2}}, \tag{5.8}$$

where $|\hat{v}|_c$ is the value of $|\hat{v}|$ at y_c^* based on an inviscid solution. From equations (7.26) and (7.37) of Benjamin (1959), a good approximation to $|\hat{v}|_c$ for a logarithmic mean-velocity profile can be found as

$$|\hat{v}|_c = \frac{ka(ky_c^*)^2 J_0 A_\infty u_*}{[1-(ky_c^*)^2 \mathrm{e}^{ky_c^*} J_1]\, k_0}. \tag{5.9}$$

Here A_∞ is determined by $|\hat{v}| = A_\infty ka(U_\infty - c)\,\mathrm{e}^{-ky^*}$ in the free stream and

$$J_0(ky_c^*) = \int_1^\infty (\ln u)^2 \exp(-ky_c^* u)\,\mathrm{d}u,$$

$$J_1(ky_c^*) = \int_1^\infty (\ln u)^2 \exp(-ky_c^* u)\, G(u)\,\mathrm{d}u,$$

with

$$G(u) = \begin{cases} \displaystyle\int_u^{u_\infty} [(\ln u)^{-2} - (\ln u_\infty)^{-2}]\,\mathrm{d}u & (u < u_\infty), \\ 0 & (u > u_\infty) \end{cases}$$

and $u_\infty = \exp[k_0(U_\infty - c)/u_*]$. The substitution of (5.9) into (5.8) then leads to

$$k\delta_m = 2(ka)^{\frac{1}{2}}(ky_c^*)^{\frac{3}{2}}\Gamma^{\frac{1}{2}}J_0^{\frac{1}{2}}, \tag{5.10}$$

where

$$\Gamma = [1-(ky_c^*)^2 e^{ky_c^*}J_1]^{-1}A_\infty. \tag{5.11}$$

The values of $k\delta_m$ for this experiment as calculated from (5.10) are listed in table 3; also included in table 3 are the values of $Z_m = y_c^*/\delta_m$, which measures the effect of the interface on the nonlinear critical layer. The values of A_∞ as determined from the observed profiles of $|\hat{v}|$ in the free stream (see figure 4) are given in table 3, together with the values of Γ determined from (5.11). Note that Γ is larger than the value of $3^{-\frac{1}{2}}$ cited on p. 104 in Phillips (1966) based on the numerical solution of Miles (1959).

From the results of $k\delta_c$, $k\delta_{ct}$ and $k\delta_m$ shown in table 3, it appears that the nonlinear critical layer plays the most significant role in determining the wave-induced flowfield; however, the effect of the turbulence on the nonlinear critical-layer structure is considerable and cannot be neglected.

From table 3, we also find that the thickness of the nonlinear critical layer for the cases of $U_\infty/c = 1.10$ and 1.36 is so very large that it does not actually represent a local scale. It is also interesting to see that for these two cases the critical layer is thicker than the wave amplitude, so that the wave-induced flow above the critical layer depends strongly on the cat's-eye pattern of the critical layer. On the other hand, the wave-induced flow above the critical layer for the cases of $U_\infty/c = 1.54$ and 1.87 depends strongly on the surface waveform because the critical layer tends to become thinner than the wave amplitude and to undulate with the waveform. More insights to this aspect are provided later.

With the above knowledge of the critical height and the critical-layer thickness, we now examine the case of $U_\infty/c = 1.10$ when both y_c^* and δ_m are comparable to the boundary-layer thickness. Under this condition, the wave-induced flow above the critical layer may depend dominantly on the undulation of the upper boundary of the cats'-eye pattern defined by

$$\tilde{y}_m^* = \delta_m|\cos\tfrac{1}{2}(kx^* - \omega t + \theta_c)| \tag{5.12}$$

(see equation (4.3.10) of Phillips 1977), where θ_c is the phase angle locating the centre of the cat's-eye. The observed $\theta_{\tilde{v}}$ shown in figure 4 indicates that $\theta_c = 180°$ when $U_\infty/c = 1.10$. It becomes questionable whether a perturbation analysis is applicable, because $\tilde{y}_m^*$ is large and comparable to $\tilde{\eta}$. The dominance of $\tilde{y}_m^*$ in determining the wave-induced flowfield above the critical layer may lead to the substantial large value in A_∞ as shown in table 3. The substantial large value of A_∞ then may lead to larger values of $|\hat{v}|_c$ and δ_m. The process is nonlinear. The solution to the wave-induced flow requires sophisticated numerical computations, but to the first approximation the analyses based on a nonlinear critical-layer theory are expected to give a qualitative description.

According to the nonlinear critical-layer theory (Benney & Bergeron 1969; Robinson 1974), the vertical velocity $\tilde{v}$ at first order is continuous across the critical layer, but $\tilde{u}$ is not. The difference in $\tilde{u}$ above and below the critical layer is $O(U_c''\delta_m^2)$ since the vorticity redistribution in the critical layer is $O(U_c''\delta_m)$. Following Phillips (1977, p. 127), the wave-associated Reynolds stress as produced by the critical layer is given by

$$-\overline{\tilde{u}\tilde{v}} = A_m\frac{|\hat{v}|_c^2}{2k}\frac{-U_c''}{U_c'} \quad (y^* < y_c^*). \tag{5.13}$$

For comparison we calculate the values of $-\overline{\tilde{u}\tilde{v}}/U_\infty^2$ by assuming $A_m = \pi$ (Miles 1957) and invoking $|\hat{v}|_c$ calculated from (5.9). The results of $|\hat{v}|_c$ (which is also used for the determination of δ_m) and $-\overline{\tilde{u}\tilde{v}}$ are listed in table 3. It is interesting to see that the value of $-\overline{\tilde{u}\tilde{v}}$ for the case of $U_\infty/c = 1.10$ as determined from (5.13) is in reasonable agreement with that given in table 2 determined from the extrapolation of the measured velocity profiles. It seems that the Miles' formula, i.e. (5.13), may describe reasonably well the production of the wave-associated Reynolds stress by the critical layer even though the critical layer is nonlinear; however, the value of $|\hat{v}|_c$ invoked in (5.13) may be substantially different from that resolved from a linear analysis (Miles 1959) because $\tilde{y}_m^*$ as given by (5.12) is substantial.

When y_c^* is high (as for the case of $U_\infty/c = 1.10$), the wave-induced flow below the critical layer is similar to that of $U_\infty/c < 1.0$, but with the additional modification due to the existence of the critical layer. The turbulent Stokes layer near the interface is compressed by the critical layer, and *vice versa*. But, when y_c^* is large, this compression may still be weak, so that the wave-induced flow below the critical layer may be represented by the superposition of the flowfields induced by the two layers, treating each separately as if one or the other did not exist. The distribution of $-\overline{\tilde{u}\tilde{v}}$ then may be described by the superposition of (5.5) and (5.13), as is also indicated in figure 5 for the case $U_\infty/c = 1.10$.

When the wind speed increases from $U_\infty/c = 1.10$ to 1.36 and 1.87, the critical height decreases rapidly from $ky_c^* = 0.47$ to 0.085 and 0.012, while the global scale of the wind (boundary-layer thickness) remains practically unchanged. The viscous sublayer becomes much thinner (inversely proportional to u_*) so that more of the upper portion of the Stokes layer is influenced by the turbulence. However, the critical height is so low that the compression of the critical layer by the interface is very severe. Two consequences are expected: (*a*) the cat's-eye becomes much more slender, undulating along the waveform as ky_c^* decreases; and (*b*) the cat's-eye becomes more uneven on the upper and lower sides of the critical height as a result of the interface compression since $ky_c^* < k\delta_m$. The compression of the flowfield below the critical layer by the interface may enhance the production of the wave-associated Reynolds stress in the critical layer.

When y_c^* is low, the component in $\tilde{u}$ produced by the critical layer, i.e. the difference between the values of $\tilde{u}$ above and below the critical layer, may become the dominant component in $\tilde{u}$ below the critical layer. This component is $O(U_c''\delta_m^2)$, and is 180° different from the phase of $\tilde{v}$ near the interface. Since $\theta_{\tilde{v}} = 270°$ near the interface, the phase of this dominant component in $\tilde{u}$ near the interface is 90°. Our observed data for $\tilde{u}$ as shown in figure 3 for the cases of $U_\infty/c = 1.36$ and 1.87 apparently support the above argument. The limit values of $|\hat{u}|$ and $\theta_{\hat{u}}$ as $ky^* \to 0$ then provide a good approximation to this dominant component in $\tilde{u}$ below y_c^*.

When y_c^* is low, most of the turbulent boundary layer is in the flow regime above the critical layer. The wave-induced flowfields above the critical layer are still dependent on the undulation of the upper boundary of the cat's-eye. However, because $k\delta_m$ may become smaller than ka, the upper boundary of the cat's-eye as referred to the Cartesian coordinate system is located at

$$\langle y_m \rangle = \langle y_c^* \rangle + \tilde{\eta}\, e^{-k\langle y_c^* \rangle} + \tilde{y}_m^*, \tag{5.14}$$

where $\tilde{y}_m^*$ is given by (5.12) and $\langle y_c^* \rangle$ is determined by $U + \tilde{u} - c = 0$. Hence $\langle y_c^* \rangle$ is a function of x^*. The change in the critical height with x^* represents the effect due to the nonlinear convection by $\tilde{u}$. To the first approximation $\langle y_c^* \rangle$ can be expressed as $\langle y_c^* \rangle = y_c^* - \tilde{u}_c/U_c'$, where $\tilde{u}_c$ is the value of $\tilde{u}$ at y_c^*. When y_c^* is small, the second

Run	$k\lvert\hat{u}\rvert_c/U'_c$	$ka\,e^{-ky^*_c}$	$0.6k\delta_m$
2	0.012	0.067	0.28
3	0.036	0.096	0.096
I‡	0.027	0.103	0.045
4	0.014	0.114	0.016

‡ The run of Hsu *et al.* (1981) referred to as I.

TABLE 4. Comparison of the amplitudes of the components contributing to the undulation of the upper boundary of cat's-eye

term on the right-hand side of (5.14) is significant because it is $O(\tilde{\eta})$. In the limit of $y^*_c \to 0$, $\langle y_m \rangle = \tilde{\eta}$ and the flow above the critical layer approaches that over a solid wavy wall. The amplitudes of the fundamental mode for each term on the right-hand side of (5.14) as normalized by k are $k|\hat{u}|_c/U'_c$, $ka\exp(-ky^*_c)$ and $0.6k\delta_m$ respectively – they are listed in table 4. In table 4, the values of $|\hat{u}|_c$ used to determine $k|\hat{u}|_c/U'_c$ are obtained from figure 3 of this study and figure 5 of I. From table 4 it is clear that the undulation of the surface wave in determining the wave-induced flowfield near the free stream becomes dominant at high wind speed when the critical height and the critical layer are smaller than the wave amplitude. Above the critical layer and near the free stream, the phase $\theta_{\tilde{v}}$ lags the phase of $\langle y_m \rangle$ by 90°; hence the phases of $\langle y_m \rangle$ as inferred from the observed $\theta_{\tilde{v}}$ are 180°, 250°, 270° and 305° for $U_\infty/c = 1.10$, 1.36, 1.54 and 1.87 respectively. Clearly, the centre of the cat's-eye is located above the trough when $U_\infty/c = 1.10$, and moves toward the wave crest along the leeward side of the wave when the wind speed increases. Owing to the displacement of the critical height by $\tilde{u}$ and the compression of the critical layer by the interface, the cat's-eye is highly asymmetric and skewed. An example of the asymmetric and skewed critical layer is given by Phillips (1977, figure 4.3). More details on this type of critical layer are provided by Gent & Taylor (1977).

In the above, we have demonstrated that when y^*_c is low the amplitude of $\tilde{u}$ near the interface is large, $O(U''_c\delta^2_m)$, and the phase of $\tilde{u}$ near the interface is close to 90°. On the other hand, the phase of $\tilde{u}$ near the free stream shifts continuously from 180° toward 360° along the leeward side of the wave when the wind speed increases. The phase of $\tilde{v}$ near the interface is 270°, as required by interface boundary condition, while the phase of $\tilde{v}$ near the free stream always lags the phase of $\tilde{u}$ near the free stream by 90°, as implied by inviscid theory. The mismatch between the phases near the interface and near the free stream is smoothed by the critical layer. If there is no turbulence, rapid changes in the phases of $\tilde{u}$ and $\tilde{v}$ may occur in the close proximity of the interface within a region of order of the critical-layer thickness centred at the critical height. However, with turbulence this smoothing process may diffuse more extensively away from the interface. The observed profiles of $\theta_{\tilde{u}}$ and $\theta_{\tilde{v}}$ for $U_\infty/c = 1.36$ and 1.87 as shown in figures 3 and 4 seem to be consequences of these smoothing and turbulent-diffusion processes. The distribution of $-\overline{\tilde{u}\tilde{v}}$ then has a positive value near the interface, decreases to a negative minimum at somewhere in the boundary layer when $\theta_{\tilde{u}} \approx \theta_{\tilde{v}}$, and increases to zero on approaching the free stream (see §4.3.2). It should be noted that the nonlinear critical layer is very diffusive since it locates in the energetic turbulent region. The fluid in the cat's-eye of the turbulent nonlinear critical layer is continuously renewed.

In summary, the interaction between the wind and the wave depends not only on the wind and the wave scales, but also on the dynamic coupling parameter U_∞/c

which determines the critical height and consequently the critical-layer thickness. When $U_\infty/c < 1.0$, the wind/wave interaction is characterized only by the wavelength k^{-1}, the wave amplitude a, the Stokes-layer thickness β^{-1}, the turbulent boundary-layer thickness δ and the viscous-sublayer thickness δ_0. They form the non-dimensional parameters ka, k/β, $k\delta_0$ and $k\delta$. (The critical height y_c^* here is regarded as at infinity, i.e. $ky_c^* = \infty$.) Under this condition, the entire turbulent boundary layer is below the critical height. For the experimental condition of this study, $k/\beta \ll ka$ so that the Stokes layer is a thin layer bent along the waveform. We also find that $k\delta \ll ka$, which implies the mean wind profile basically follows the waveform. For this study, $k\delta \approx 1.0$; hence the wave-induced flow in the region $0 < ky^* < 1.0$ is strongly affected by the wind shear while that in $ky^* > 1.0$ behaves as that of a potential flow. Because $k/\beta \approx k\delta_0$, the upper portion of the Stokes layer is modified by turbulent diffusion so that the turbulent Stokes-layer thickness is comparable to the wave amplitude. This also leads to the oscillatory profile of $-\overline{\tilde{u}\tilde{v}}$ as observed in this experiment.

When $U_\infty/c > 1.0$ but $ky_c^* = O(k\delta)$, the wave-induced flow in the region $ky^* > 1.0$ is still potential flow but is dependent on the undulation of the cat's-eye pattern associated with the critical layer. The critical layer is nonlinear and turbulently diffusive; the critical-layer thickness is large compared with the wave amplitude, i.e. $k\delta_m > ka$. The flow below the critical layer is still mainly in the turbulent boundary layer and behaves as if it were that in an undulating channel bounded by the wave surface and the lower boundary of the cat's-eye, except that the boundary condition at the lower bundary of the cat's-eye depends on the structure of the cat's-eye pattern, which cannot be known *a priori*. The cortical layer probably works as if it were an upper barrier in confining the diffusion of the turbulent Stokes layer, and on the other hand generates some additional wave-associated Reynolds stress due to the transport of vorticity when the fluid circulates around the cat's-eye. The effect on the Stokes layer by turbulent mixing is still dominant compared to that by critical-layer compression. Hence the distribution of $-\overline{\tilde{u}\tilde{v}}$ in the boundary layer is similar to that for the case of $U_\infty/c < 1.0$, but differs by a constant value of $-\overline{\tilde{u}\tilde{v}}$ given by (5.13).

When the wind speed is further increased that $ky_c^* \ll O(ka)$, the critical layer becomes a thin layer bending along the waveform in the proximity of the interface. The turbulent boundary layer is mostly above the critical layer. The region below the critical layer is so thin that the wave-induced flow near the interface is predominantly determined by the critical layer. The wave-induced flow near the free stream on the other hand is predominantly determined by the surface waveform. These two characteristics near the interface and the free stream are linked in the turbulent boundary layer through turbulent mixing.

Apparently, there exists a value of U_∞/c which distinguishes the flow regime of low critical level from that of high critical level. Our observations of this study indicate that this value may be located at somewhere near $U_\infty/c = 1.36$, when $ky_c^* = O(ka)$. Under this circumstance, the critical layer is not only significant in determining the wave-induced flowfield near the free stream, but has also become predominant in determining the wave-induced flowfields near the interface. The flow regime of low critical level seems to be signified by the phase jump of 180° in the profiles of $\theta_{\tilde{r}_{ij}}$ as observed for the cases of $U_\infty/c = 1.54$ and 1.87.

6. Conclusions

This study extends our earlier experimental works (Hsu *et al.* 1981) on $U_\infty/c = 1.54$ to the cases $U_\infty/c = 0.88$, 1.10, 1.36 and 1.87 by changing the speed of the turbulent air flow, while the mechanically generated water surface wave was maintained at 1 Hz with the wave slope approximately equal to 0.1. The consistency between the results of the present experiment with our earlier results was established, since they applied the same data-taking technique (measurements in the wave-following coordinate system) and the same data-reduction scheme. The results of the experiment in the context of several theoretical analyses suggests the following.

(1) The turbulent wind-velocity profiles over the mechanically generated water wave basically follow the waveform. The surface condition for the flow in this study is regarded as super-smooth because the mean turbulent shear stress supported by the surface drift current is relatively lower than that supported by a smooth flat plate.

(2) The structure of the wave-induced velocity fields depends strongly on the height of the critical layer. Because the critical height changes exponentially with c/u_* as a consequence of a log-linear mean-velocity profile, the structure of the wave-induced velocity fields depends very strongly on the parameter U_∞/c.

(3) When the critical height is high (the cases of $U_\infty/c = 0.88$ and 1.10 in which the turbulent boundary layer is mainly below the critical layer), the structure of the wave-induced velocity fields is affected drastically by the Stokes layer at the interface. The Stokes layer is considerably thickened by turbulent mixing. Hence the oscillatory characteristics of the wave-associated Reynolds stress $-\overline{\tilde{u}\tilde{v}}$ can extend to a significant height before it decays to negligible level.

(4) When the critical height is low (the cases $U_\infty/c = 1.36$, 1.54 and 1.87 so that the turbulent boundary layer is mainly above the critical layer), the wave-induced velocity near the free stream depends predominantly on the undulations of the critical height and the upper boundary of the cat's-eye. On the other hand, the wave-induced velocity in close proximity to the interface is determined strongly by the compression of the flowfields below the critical layer by the critical layer and the interface, and by the interface boundary condition. The effect of turbulence is then to link these wave-induced velocities near the interface and the free stream to yield continuously varying profiles.

(5) The critical layer is nonlinear and is turbulently diffusive. The thickness of the turbulent nonlinear critical layer is larger than the wave amplitudes when the critical height is high. The critical layer becomes thinner than the wave amplitudes and bends along the waveform when the critical height is lower than the wave amplitudes.

(6) Miles' formula, i.e. (5.13) with $A_m = \pi$, seems to be applicable when the critical level is not too low (the cases $U_\infty/c = 1.10$ and 1.36); however, the value of Γ used to infer the value of $|\hat{v}|_c$ has to be determined directly from the measurements rather than from the numerical computations of a quasi-laminar model. When the critical layer is low (the cases $U_\infty/c = 1.54$ and 1.87), Miles' formula even with the experimental evaluation of Γ underpredicts the wave-supported stress $-\overline{\tilde{u}\tilde{v}}$ by a factor of two to three.

(7) While the frictional drag $-\overline{u'v'}$ has a constant-stress layer below $ky^* < 0.5$ and outside the viscous sublayer (see figure 4 of I), the waveform drag $-\overline{\tilde{u}\tilde{v}}$ is observed to change drastically in the constant-stress layer of $-\overline{u'v'}$. As a result, the total stress $-(\overline{u'v'} + \overline{\tilde{u}\tilde{v}})$ exerted by the turbulent wind on the interface does not provide a constant-stress layer above the interface.

(8) The response of the turbulent Reynolds stresses to the wave depends on the

flow regimes near the interface or in the boundary layer. Near the interface, the wave-induced turbulent Reynolds stresses are produced from the stretching and changing in the direction of the turbulent velocity fluctuations due to the surface displacements. Hence the maximum turbulent intensity occurs at the wave crests, where the stretching effect is maximum, and the maximum shear $\langle u'v' \rangle$ occurs at the positions of maximum wave slope, where the change in the direction of the velocity fluctuation is maximum. In the boundary layer, the relations between the wave-induced turbulent Reynolds stresses and the wave-induced velocities are basically of an eddy-viscosity type, with the wave-induced turbulent intensity governed by the acceleration and deceleration processes of the phase-average flow observed in the frame travelling with the wave celerity.

(9) The inclusion of both the nonlinear and turbulent effects on the wave-induced flowfields is essential to the success of numerical modelling.

This work was supported by the National Science Foundation through Grant No. OCE-8100517. The experimental data were obtained when the first author was at the Department of Civil Engineering, Stanford University.

Appendix

A model of the turbulent Stokes layer

By Russ E. Davis (Scripps Institution of Oceanography, La Jolla)

As suggested by Hsu & Hsu (HH) in §5.2, modelling of a laterally homogeneous oscillating turbulent boundary layer can be approached by assuming that the effective viscosity is the sum of the molecular viscosity, ν, and the eddy viscosity obtained from the law of the wall. If the fluctuating downstream velocity is $u = \mathrm{Re}\,[U(y)\exp(\mathrm{i}\omega t)]$ then the additive-viscosity model leads to

$$\mathrm{i}\omega U = \frac{\mathrm{d}}{\mathrm{d}y}(\nu + \kappa u_* z)\frac{\mathrm{d}}{\mathrm{d}y}U, \tag{A 1}$$

where κ is von Kármán's constant and u_* is the friction velocity. The auxiliary conditions for (A 1) are that U vanish as $y \to \infty$ and that U, U', or some combination of the two, be specified at $y = 0$. Let

$$\lambda = \frac{\kappa u_*}{4|\omega|}, \quad z_0 = \frac{\nu}{u_*\kappa}, \quad \eta = \frac{y + z_0}{\lambda}, \quad \mu = \frac{\omega}{|\omega|}.$$

If $F(\eta)$ is a solution of

$$\frac{\mathrm{d}}{\mathrm{d}\eta}\left(\eta\frac{\mathrm{d}}{\mathrm{d}\eta}F\right) = 4\mathrm{i}\mu F, \quad \lim_{\eta\to\infty} F = 0, \tag{A 2}$$

then $U(y)$ is some multiple of $F((y+z_0)/\lambda)$; the condition $U(y=0) = U_0$ corresponds to

$$U(y) = U_0 F\left(\frac{y+z_0}{\lambda}\right)\Big/F\left(\frac{z_0}{\lambda}\right).$$

Transforming the independent variable in (A 2) to $\eta^{\frac{1}{2}}$ converts that equation to (9.9.3) of Abramowitz & Stegun (1964) (AS) with the solution

$$F(\eta) = K_0(\eta^{\frac{1}{2}}\mathrm{e}^{\frac{1}{4}\mathrm{i}\mu\pi}),$$

where K_0 is the zeroth-order modified Bessel function with $\lim_{x\to\infty} K_0(x) = 0$.

For $\eta \ll 1$ an approximate representation

$$F(\eta) = -\tfrac{1}{2}[(1+\tfrac{1}{4}\mathrm{i}\mu\eta)\ln\eta + \tfrac{1}{2}\mathrm{i}\mu\pi - 0.232] + O(\eta) \tag{A 3}$$

may be obtained from AS (9.6.13). This shows that for $y \ll \lambda$ the velocity profile is logarithmic and phase variation occurs on the scale 4λ. For $\eta \gg 1$ an approximate representation

$$F(\eta) = \exp[-1+\mu\mathrm{i})(\tfrac{1}{2}\eta)^{\frac{1}{2}} - \tfrac{1}{8}\mathrm{i}\mu\pi] \tag{A 4}$$

may be obtained from AS (9.7.2). This will be recognized as a close relative of the classical constant-viscosity Stokes-layer solution. The exact amplitude and phase of the function $F(\eta)$ can be determined from figure 9.11 and table 9.12 of AS with the substitution amplitude $[F(\eta)] = N_0(\eta^{\frac{1}{2}})$ and phase $[F(\eta)] = \phi_0(\eta^{\frac{1}{2}})$.

In §5.2, HH use this model to interpret observations of the wave-associated Reynolds stress in light wind flow over a water wave with amplitude a and wavenumber k. In (5.3) HH show that, because the turbulent stresses affect the normal velocity component $\tilde{v}$ only slightly, the wave-associated Reynolds stress $-\overline{\tilde{u}\tilde{v}}$ should vary as

$$-\overline{\tilde{u}\tilde{v}} = (akc)^2 \mathrm{e}^{-ky^*} \operatorname{Im}[U(y^*)], \tag{A 5}$$

where y^* is the wave-following normal coordinate and U is the solution of (1) with $U(0) = 1$. HH's (5.5) is an approximation (A 5) based on the large-η form (A 4) in which the factor $\eta^{-\frac{1}{2}}$ has been replaced by the adjustable constant A_0. By comparing this approximation with the results of their $U_\infty/c = 0.88$ experiment, HH find support for the additive-viscosity model. Since this is an important result it seems crucial to examine the comparison with the exact solution, particularly since the experiment corresponds to $z_0/\lambda = 1.3$, which is not large.

The approximation (5.5) predicts the first negative minimum of $-\overline{\tilde{u}\tilde{v}}$ to occur at $\frac{1}{2}\eta = (\frac{5}{4}\pi)^2$, or $ky^* = 0.12$, which is in good agreement with observation. Examination of figure 9.11 of AS shows that the phase of F varies almost exactly as $(\frac{1}{2}\eta)^{\frac{1}{2}}$ for values of $\eta > 0.5$, so that agreement between the observed position of the stress extremum and the exact solution is good. The magnitude of the observed stress at the extremum is, however, four times larger than that predicted by this solution. Even the approximation (5.5), which does not include the $\eta^{-\frac{1}{2}}$ decrease of amplitude found in (A 4), requires the unrealistic choice $A_0 = 2.5$ to match the observations (HH apparently erred in stating that a value of 1.5 was sufficient). It must be concluded therefore that the additive-viscosity model is only qualitatively correct and the agreement obtained may be only coincidental.

It might be noted that the exact solution above is directly applicable to oscillating boundary layers in a rotating frame. In this case the velocity parallel to the boundary is represented as $u_1 + \mathrm{i}u_2 = U(y = x_3)\exp(\mathrm{i}\omega' t)$, and (A 1) holds with the substitution $\omega = \omega' + f$, where f is the Coriolis parameter.

REFERENCES

Abramowitz, M. & Stegun, I. A. 1964 *Handbook of Mathematical Functions.* Natl Bureau of Standards.

Benjamin, T. B. 1959 Shearing flow over a wavy boundary. *J. Fluid Mech.* **6**, 161–205.

Benney, D. J. & Bergeron, R. F. 1969 A new class of nonlinear waves in parallel flows. *Stud. Appl. Maths* **48**, 181–204.

Csanady, G. T. 1974 The 'roughness' of the sea surface in light winds. *J. Geophys. Res.* **79**, 2747–2751.

DAVIS, R. E. 1969 On the high Reynolds number flow over a wavy boundary. *J. Fluid Mech.* **36**, 337.

DAVIS, R. E. 1972 On prediction of the turbulent flow over a wavy boundary. *J. Fluid Mech.* **52**, 287–306.

DAVIS, R. E. 1974 Perturbed turbulent flow, eddy viscosity and the generation of turbulent stresses. *J. Fluid Mech.* **63**, 673–693.

GENT, P. R. & TAYLOR, P. A. 1977 A note on 'separation' over short wind waves. *Boundary-Layer Met.* **11**, 65–87.

HINZE, J. O. 1975 *Turbulence – An Introduction to Its Mechanism and Theory.* McGraw-Hill.

HSU, C. T., HSU, E. Y. & STREET, R. L. 1977 The structure of modulated turbulent flow over progressive water waves. *Stanford Univ. Dept Civ. Engng Rep.* no. 221.

HSU, C. T., HSU, E. Y. & STREET, R. L. 1981 On the structure of turbulent flow over a progressive water wave: theory and experiment in a transformed, wave-following coordinate system. *J. Fluid Mech.* **105**, 87–117.

HSU, C. T., HSU, E. Y. & STREET, R. L. 1982 On the transfer of wind momentum and energy across an interface with a progressive water wave. (Unpublished manuscript.)

HUSSAIN, A. K. M. F. & REYNOLDS, W. C. 1970 The mechanics of an organized wave in turbulent shear flow. *J. Fluid Mech.* **41**, 241–258.

LIN, C. C. 1955 *The Theory of Hydrodynamic Stability.* Cambridge University Press.

MILES, J. W. 1957 On the generation of surface waves by shear flows. *J. Fluid Mech.* **3**, 185–204.

MILES, J. W. 1959 On the generation of surface waves by shear flows. Part 2. *J. Fluid Mech.* **6**, 568–582.

MILES, J. W. 1967 On the generation of surface waves by shear flows. Part 5. *J. Fluid Mech.* **30**, 163–175.

PHILLIPS, O. M. 1966 *The Dynamics of the Upper Ocean*, 1st edn. Cambridge University Press.

PHILLIPS, O. M. 1977 *The Dynamics of the Upper Ocean*, 2nd edn. Cambridge University Press.

PORTMAN, D. J. 1960 An improved technique for measuring wind and temperature profiles over water and some results obtained for light winds. *Great Lakes Res. Div., Univ. Michigan, Ann Arbor, Publ.* 4, pp. 77–84.

ROBINSON, J. L. 1974 The inviscid nonlinear instability of parallel shear flows. *J. Fluid Mech.* **63**, 723–752.

SHEPPARD, P. A., TRIBBLE, D. T. & GARRETT, J. R. 1972 Studies of turbulence in the surface layer over water. *Q. J. R. Met. Soc.* **98**, 627–641.

TENNEKES, H. & LUMLEY, J. L. 1972 *A First Course in Turbulence.* MIT Press.

TOWNSEND, A. A. 1972 Flow in a deep turbulent boundary layer over a surface distorted by water waves. *J. Fluid Mech.* **55**, 719–753.

WU, J. 1975 Wind-induced drift currents. *J. Fluid Mech.* **68**, 49–70.

YU, H. Y., HSU, E. Y. & STREET, R. L. 1973 Wave-induced perturbations in a turbulent boundary layer over progressive water waves. *Stanford Univ. Dept Civ. Engng Rep.* no 172.